

ARTICLE

MYO1F in neutrophils is required for the response to immune checkpoint blockade therapy

Yingying Qu^{1,2,3}*, Wenhua Liang^{1,3}*, Mingzhu Yu^{1,3}, Chenhui Wang⁴, Min Luo⁵, Lin Zhong^{6,7}, Zhigang Li⁸, and Feng Wang^{1,3}

Tumor-associated neutrophils (TANs) represent a significant barrier to the effectiveness of immune checkpoint blockade (ICB) therapy. A comprehensive understanding of TANs' regulatory mechanisms is therefore essential for predicting ICB efficacy and improving immunotherapy strategies. Our study reveals that MYO1F is selectively downregulated in neutrophils within both human cancers and murine tumor models, showing a negative correlation with ICB response. Mechanistically, MYO1F normally inhibits neutrophil immunosuppression and proliferation by restraining STAT3 activity. However, during tumorigenesis, tumorderived TGF-β1 disrupts the binding of SPI1 to intron 8 of *Myo1f* via DNA methylation, thereby suppressing *Myo1f* transcription. The resultant decrease in MYO1F reprograms neutrophils into an immunosuppressive state through the STAT3-dependent signaling pathways. This immunosuppressive state further contributes to tumor microenvironment (TME) remodeling by inducing CTL exhaustion. These findings establish MYO1F as a critical regulator within TANs, highlighting its significant role in modulating ICB therapy efficacy.

Introduction

Low response of immune checkpoint blockade (ICB) is an important obstacle to immunotherapies. In cancer, heterogeneous neutrophils released from the bone marrow (BM) have emerged as important components of the tumor microenvironment (TME) (Jaillon et al., 2020; Quail et al., 2022) with high plasticity and display protumorigenic functions. Tumor-associated neutrophils (TANs) are defined by the surface expression of CD11b+Ly6ClowLy6Ghigh in mice and CD11b+CD14lowCD33high in humans. Fridlender et al. (2009) suggested that TGF-β1, an immunosuppressive cytokine expressed by tumor cells, could transform TANs from anti-tumorigenic neutrophils (N1) into protumorigenic neutrophils (N2) (Fridlender et al., 2009). Most neutrophils in tumor appear to have an N2 phenotype and thus contribute to tumor growth and immunosuppression (Antuamwine et al., 2023; Chung et al., 2021; Shojaei et al., 2008; Yin et al., 2022; Zhang et al., 2024). N2 neutrophil depletion led to a decrease in tumor growth in mouse models (Fridlender et al., 2009). Although TGF-β1-mediated N2 neutrophils are involved in the immunosuppression in most solid tumors, the

underlying molecular mechanism is not fully understood. High levels of N2 neutrophils are indicative of a poor response to ICB therapies, such as ipilimumab and nivolumab (de Coaña et al., 2017; Martens et al., 2016; Sade-Feldman et al., 2016), particularly in patients with nonresectable melanoma (Weber et al., 2016), which was mainly attributed to potent immunosuppression and continuous expansion. Unraveling the molecular mechanisms behind these decisive events is a prerequisite for the development of therapy targeting neutrophils.

For immunosuppression, N2-like neutrophils play a pivotal role in facilitating tumor immune evasion by remodeling the TME through a variety of mediators, including ROS, arginase 1 (ARG1), inducible nitric oxide synthase (NOS2), IL-10, and indoleamine 2,3-dioxygenase 1 (IDO1), which collectively suppress effector T cell activity (Gabrilovich and Nagaraj, 2009). ROS has emerged as one of the main characteristics of neutrophils in both tumor-bearing mice and patients with cancer (Kusmartsev et al., 2004; Schmielau and Finn, 2001). The inhibition of ROS production in neutrophils isolated from mice and

¹Institute of Pediatric Infection, Immunity, and Critical Care Medicine, Shanghai Children's Hospital, Shanghai Jiao Tong University School of Medicine, Shanghai, China; ²Center for Microbiota and Immunological Diseases, Shanghai General Hospital, Shanghai Jiao Tong University School of Medicine, Shanghai, China; ³Shanghai Institute of Immunology, Department of Immunology and Microbiology, State Key Laboratory of Oncogenes and Related Genes, Shanghai Jiao Tong University School of Medicine, Shanghai, China; ⁴The Key Laboratory for Human Disease Gene Study of Sichuan Province and the Department of Laboratory Medicine, Sichuan Provincial People's Hospital, University of Electronic Science and Technology of China, Chengdu, China; ⁵Institute of Pediatrics of Children's Hospital of Fudan University, The Shanghai Key Laboratory of Medical Epigenetics, The International Co-laboratory of Medical Epigenetics and Metabolism, Ministry of Science and Technology, Institutes of Biomedical Sciences, Fudan University, Shanghai, China; ⁶Department of Liver Surgery and Organ Transplantation Center, Shenzhen Third People's Hospital, Second Affiliated Hospital, Southern University of Science and Technology, Shenzhen, China; ⁷Department of General Surgery, Shanghai General Hospital, Shanghai Jiao Tong University School of Medicine, Shanghai, China; ⁸Department of Thoracic Surgery, Shanghai Chest Hospital, Shanghai Jiao Tong University School of Medicine, Shanghai, China.

*Y. Qu and W. Liang contributed equally to this paper. Correspondence to Feng Wang: wangfeng16@sjtu.edu.cn.

© 2025 Qu et al. This article is distributed under the terms as described at https://rupress.org/pages/terms102024/.





tumor patients completely abrogated the suppressive effect of these cells in vitro (Kusmartsev et al., 2004; Szuster-Ciesielska et al., 2004).

For expansion, neutrophil heterogeneity also exists in the BM in the form of various precursors and maturation stages. Tumorinduced chronic inflammation triggers the expansion of neutrophils via activation of the STAT3 signaling pathway and premature egress of these precursors into the circulation and subsequently infiltrating into the tumor (Evrard et al., 2018; Khoyratty et al., 2021; Ng et al., 2019), which has emerged as a significant barrier to ICB response (Bronte et al., 2001; Jiang et al., 2015; Jordan et al., 2013; Meyer et al., 2014; Morad et al., 2022; Weide et al., 2014). Ablation of STAT3 expression in conditional KO mice or selective STAT3 inhibitors markedly reduce the expansion of neutrophils and increase T cell antitumor responses (Kortylewski et al., 2005; Nefedova et al., 2005).

The long-tailed unconventional class I myosin, myosin 1F (MYO1F), has been proposed to play a role in the migration and polarization of neutrophils, macrophages, and dendritic cells (DCs) (Kim et al., 2006; Navinés-Ferrer et al., 2019; Teixeira, 2018; Wang et al., 2021b). Interestingly, deficiency of MYO1F induced by gene fusion or mutation has been implicated in infant acute monocytic leukemia and thyroid cancer, indicating a direct involvement of MYO1F in cell proliferation (Diquigiovanni et al., 2018; Duhoux et al., 2011; Taki et al., 2005). However, our understanding of the impact of MYO1F in myeloidderived cells during tumor progression is still in its infancy. MYO1F and MYO1E, which are the only two long-tailed type I myosin proteins that exhibit high structural and functional similarity, perform essential roles in various physiological processes, such as endocytosis, exocytosis, cell adhesion, and migration (McConnell and Tyska, 2010; Navinés-Ferrer and Martín, 2020).

In this study, we examined databases with information on the clinical response to ICB therapy and identified a correlation between reduced expression of MYO1F and a poor response to ICB therapy. Further research revealed that MYO1F was highly expressed in neutrophils and restrained the amplification of neutrophils under normal physiological conditions via MYO1F/ TRIM21/prohibitin 1 (PHB1) axis. During tumorigenesis, tumorderived TGF-β1 can specifically downregulate Myo1f expression in BM neutrophils by interfering with the binding of SPI1 to intron 8 of Myolf. The reduced MYO1F level triggered the proliferation of pathologically activated neutrophils through STAT3-ROS/PD-L1 signaling pathways. These neutrophils possessing high immunosuppressive ability remodeled the TME by inducing CTL exhaustion. Our study revealed that the MYO1F is pivotal in restricting both quality and quantity of TANs to improve the ICB efficacy.

Results

MYO1F level is a predictive biomarker for the outcome of ICB therapy

To seek possible predictors for ICB treatment, we profiled gene expression in samples from patients in the Tumor Immunotherapy Gene Expression Resource (TIGER) (Chen et al., 2023) and The Cancer Genome Atlas (TCGA) database to comprehensively investigate gene expression of tumor tissue during ICB treatment (Chen et al., 2023). Based on the investigation from two databases, we found that low expression of MYO1F, but not MYO1E, was associated with a poor response to ICB therapy and a poor survival rate in a dataset of patients with melanoma treated with αPD-1 and αCTLA-4 immunotherapy (Fig. 1 A and Fig. S1, A-C). Given that low expression of MYO1F presented clinical correlation with tumor progression (Diquigiovanni et al., 2018; Duhoux et al., 2011; Taki et al., 2005) without corresponding mechanisms support, this piqued our interest in the potential role of MYO1F in tumor progression and ICB resistance. To verify the above findings, we used another immunotherapy database, the ICBatlas (Yang et al., 2022). Consistently, lower MYO1F in tumor tissue was observed in the nonresponse datasets of multiple solid cancer types (Fig. S1, D and E). Thus, a low level of MYO1F might be an indicator of a poor response to ICB therapy.

To determine the role of MYO1F in tumor, we analyzed the MYOIF expression level in clinical tumor tissues and normal tissues from the TCGA database via the GEPIA2 website (Tang et al., 2019). Lower MYOIF expression in tumor tissue was observed in 18 cancer types, and liver hepatocellular carcinoma served as representative examples (Fig. 1 B). Besides, high level of MYO1F is correlated with lower survival hazard ratio (Fig. 1 C); correspondingly, low expression of MYO1F was accompanied by a lower survival rate represented by sarcoma as a typical example (Fig. 1 D). Additionally, we compared MYO1F expression between normal and tumor tissues from the same patient and found that MYOIF expression was significantly reduced in tumor tissue (Fig. S1 F). In contrast, no obvious difference in MYO1E gene expression was observed within the same sample set. Low levels of MYO1F were also verified by immunofluorescence staining of a 45-sample melanoma tissue Chromatin Immunoprecipitation (CHIP) (Fig. 1 E). The above clinical data indicated that the MYO1F level could affect tumor progression and the response to ICB therapy.

To investigate the role of MYO1F in tumor cells, we used shRNA to knock down Myolf in the B16F10 and MC38 tumor cell lines (Fig. S1 G). Interestingly, we found no significant difference in the tumor growth or the response rate to ICB treatment after Myolf knockdown (Fig. 1, F and G; and Fig. S1, H and I). These data led us to speculate that MYO1F may affect tumor progression and the response to ICB therapy by directly modulating immune cell function rather than tumor cell function. We then used Myolf KO mice to assess the overall impact of MYO1F on the response to ICB therapy. To mimic ICB therapy in melanoma patients, αCTLA-4 and αPD-1 ICB treatments were administered to KO mice bearing B16F10 melanoma tumors. Compared with WT mice, which responded positively to treatment, KO model mice exhibited poorer responses to ICB treatment (Fig. 1 H). These data indicate that MYO1F is not a tumor suppressor gene directly but rather a contributor to the response to ICB therapy through manipulation of anti-tumor immune components.



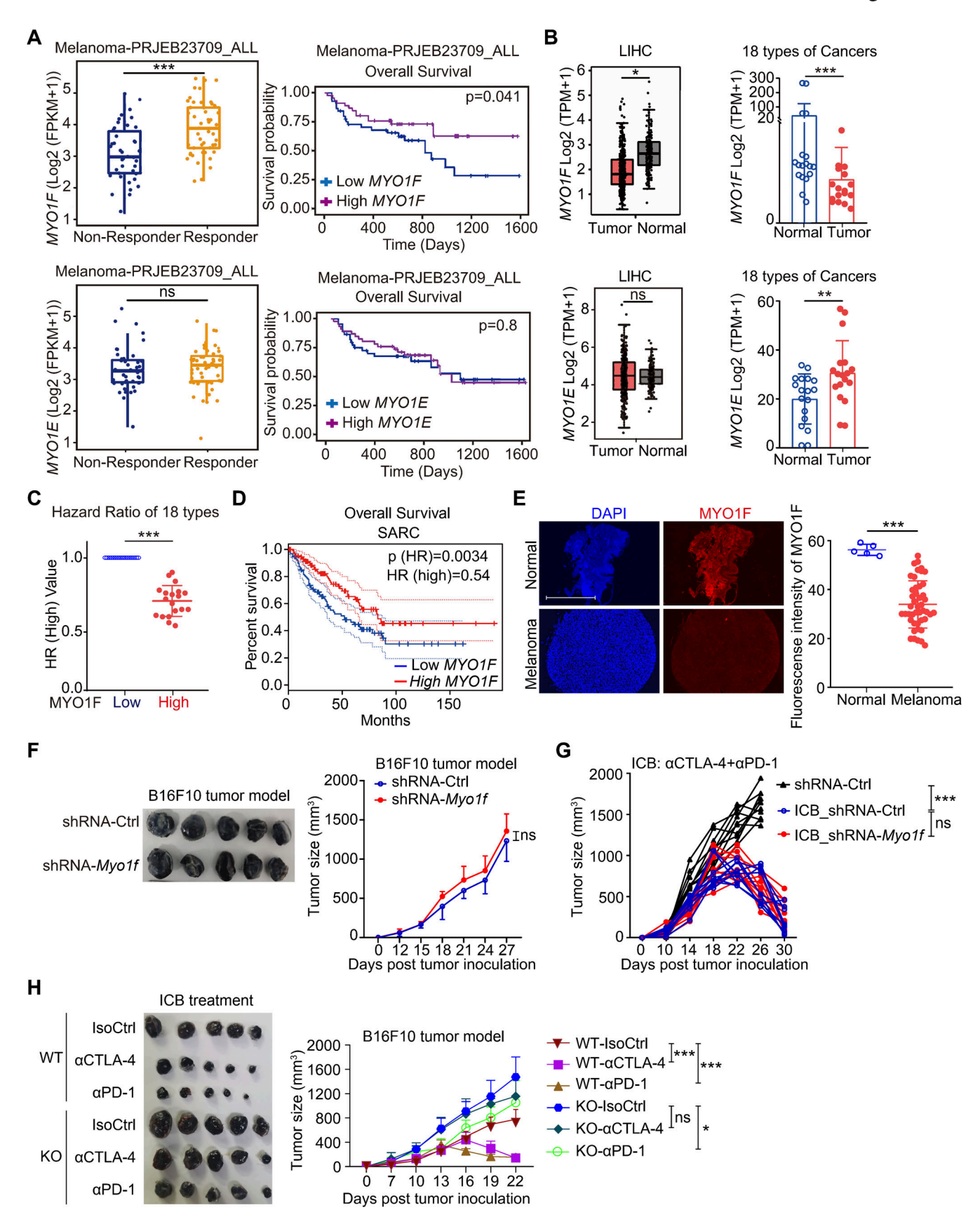


Figure 1. The expression level of MYO1F is correlated with the efficacy of ICB therapy in both humans and mice. (A) Left: MYO1F and MYO1E gene expression of tumor tissue pooled from responder (N = 49) and nonresponder (N = 42) of PRJEB23709_anti-CTLA-4 + anti-PD-1 datasets. Right: The corresponding Kaplan-Meier survival curves. Data are from the TIGER database. (B) Left: MYO1F and MYO1E gene expression pooled from liver hepatocellular



carcinoma (LIHC) tumor tissues (N = 369) and normal tissues (N = 160). Right: MYO1F and MYO1E gene expression pooled from 18 types of tumor tissues and normal tissues from the TCGA database via the GEPAI2 website. Gene level in normal tissue was normalized to 1. The 18 cancers are: adrenocortical carcinoma (ACC), bladder urothelial carcinoma (BLCA), breast invasive carcinoma (BRCA), cervical squamous cell carcinoma and endocervical adenocarcinoma (CESC), colon adenocarcinoma (COAD), lymphoid neoplasm diffuse large B cell lymphoma (DLBC), kidney chromophobe (KICH), LIHC, lung adenocarcinoma (LUAD), lung squamous cell carcinoma (LUSC), ovarian serous cystadenocarcinoma (OV), pheochromocytoma and paraganglioma (PCPG), prostate adenocarcinoma (PRAD), rectum adenocarcinoma (READ), thyroid carcinoma (THCA), thymoma (THYM), uterine corpus endometrial carcinoma (UCEC), and uterine carcinosarcoma (UCS). (C) Hazard ratio with high and low expression levels of MY01F in tumor tissue from 18 types of cancers; ratio in low MY01F tissues was normalized to 1. The data are from TCGA database via the GEPAI2 website. (D) Kaplan-Meier survival curves of sarcoma. SARC, sarcoma. The data are from the TCGA database via the GEPAI2 website, N (high) = 131; N (low) = 131. (E) Left: Immunofluorescence staining of MYO1F on human normal and melanoma tissue. DAPI used for cell nucleus indication. Right: Statistical value of MYO1F fluorescence intensity, normal, N = 5; tumor, N = 45. Scale bar: 500 µm. (F) Left: Tumor tissues were collected. Right: Tumor growth curve over time following subcutaneous injection of 2 × 105 WT and shRNA-Myo1f B16F10 cells into immunocompetent C57BL/6 mice (N = 5). (G) Tumour growth curve over time after inoculation. Immunocompetent C57BL/6 mice were subcutaneously injected with 2 × 105 WT and shRNA-Myo1f B16F10 cells, following with administered intraperitoneally of anti-PD-1 (10 mg/kg)/ anti-CTLA-4 (10 mg/kg) antibodies on days 10, 14, and 18 (N = 10 in each group). After the treatment with antibodies, tumors were extracted and photographed. (H) Left: Tumor tissues were collected. WT and Myo1f^{-/-} C57BL/6 mice were subcutaneously injected with 2 × 10⁵ B16F10 cells. Anti-PD-1 (10 mg/kg) and anti-CTLA-4 (10 mg/kg) were administered intraperitoneally on days 10, 14, and 18 (N = 5 in each group). Right: The corresponding tumor growth over time. Data in F-H represent one experiment of three independent repeats, and E represents one experiment of two independent repeats. Data are presented as mean ± SD. P values were analyzed by one-way ANOVA test (F-H); nonparametric Wilcoxon matched-pairs signed-rank test (A and B); Kaplan-Meier (D); and two-tailed unpaired Student's t test (C and E); $^{*}P < 0.05$, $^{**}P < 0.01$, and $^{***}P < 0.001$. ns, no significance.

MYO1F deficiency induced the accumulation of TANs to promote tumor progression

To investigate the role of MYO1F in tumor progression, WT and KO mice were subcutaneously injected with murine B16F10 or MC38 tumor cells. Compared with WT mice, KO mice developed significantly larger tumors and had shorter survival times (Fig. 2, A–C; and Fig. S2, A–C). We then used flow cytometry to investigate changes in tumor-infiltrating immune cells. Among the tumor-infiltrating immune cells, CD8+ T cell exhibited weakened anti-tumor function (reduced IFN- γ and GZMB), with an increased proportion and cell number of CD11b+Gr1+ population (Fig. 2 D). According to the presence of Ly6C and Ly6G, further characterization revealed that the CD11b+Ly6G+ neutrophil subset accounted for more than twofold increase in KO mice (Fig. 2 E and Fig. S2 D).

Previous studies have shown that increased TANs during tumor progression is accompanied by splenomegaly (Browne, 2015; Ravindranathan et al., 2018). Notably, the KO tumorbearing mice presented significant splenomegaly, with an average 2.5-fold increase in spleen weight (Fig. S2 E). As shown in Fig. 1 E, the MYO1F level was decreased in melanoma tissues. To verify whether a low level of MYO1F is associated with high tumor infiltration of neutrophils in humans, we performed immunofluorescence staining for two typical human TAN markers (Poschke and Kiessling, 2012) on 45-sample melanoma tissue CHIP. As expected, neutrophils accumulated extensively in melanoma than normal tissues (Fig. 2, F and G). Moreover, high infiltration of neutrophils was associated with the lower level of MYO1F (Fig. S2 F).

To verify whether tumor-infiltrating neutrophils are the main functional cell type that lead to tumor progression in MYO1F-deficient mice, intratumoral CD45.1+CD11b+Ly6G+ neutrophils from the tumor tissues of the WT or KO B16F10 tumor-bearing mice were sorted and transferred to the irradiated tumor-bearing recipients (Fig. 2 H and Fig. S2 G). Prior to transplantation, the MYO1F expression level was verified via western blotting (Fig. S2 H), and the irradiated tumor-bearing recipients were detected to exclude the influence of self-BM (Fig. S2 I). Given the short lifespans of TANs (Ng et al., 2024;

Pillay et al., 2010), the isolated neutrophils were injected every 4 days into recipients in equal quantities. Compared with the group transferred with WT tumor-derived neutrophils, the group transferred with KO tumor-derived neutrophils presented increased tumor growth (Fig. 2 I) and downregulation of activation markers of tumor-infiltrating CD8+ T cell, such as Ki-67, IFN-γ, and GZMB (Fig. S2 J). We also observed the transferred CD45.1+ neutrophil counts for more at both proportion and absolute number in the KO donation (DON) group than the WT DON group (Fig. S2 K). These findings suggested that MYO1F-deficient tumor-infiltrating neutrophils contributed to tumor progression.

Neutrophils are pathologically expanded in the BM and are recruited to tumors through CXCR1/2 chemokine gradients (Davis et al., 2017; Lang et al., 2018). To further assess the importance of the trafficking of neutrophils for tumor infiltration in MYO1F-deficient mice, we treated B16F10 tumor cell-inoculated mice with SX-682, an effective CXCR1/2 inhibitor that blocks the recruitment of neutrophils from the BM to tumors. The proportion of tumor-infiltrating neutrophils did not significantly differ between WT and KO mice after SX-682 treatment (Fig. S2 L), followed by no significant differences in tumor growth (Fig. 2 J) or survival rates (Fig. S2 M). Moreover, we found that SX-682 treatment also rescued GZMB production of CD8+T cell from KO mice (Fig. 2 K).

Finally, we aimed to determine the cause of the increased infiltration of neutrophils in tumors under the context of MYOIF deficiency. Given the potential role of MYOIF in cell mobility, we wondered whether the increase of assembled tumorinfiltrating neutrophils was due to enhanced migration ability. However, the results of the chemotaxis assay revealed no significant difference in migration between neutrophils isolate from WT tumor tissues and those from KO (Fig. S3 A).

Given that TANs are short-lived effector cells, continuous release from the BM into tumors is necessary to maintain their immunosuppressive function. We analyzed BM cells by flow cytometry and confirmed a significant, approximately twofold increase in the proportion and numbers of CD11b+Ly6G+ neutrophils in KO tumor-bearing mice (Fig. 2 L and Fig. S3 B).



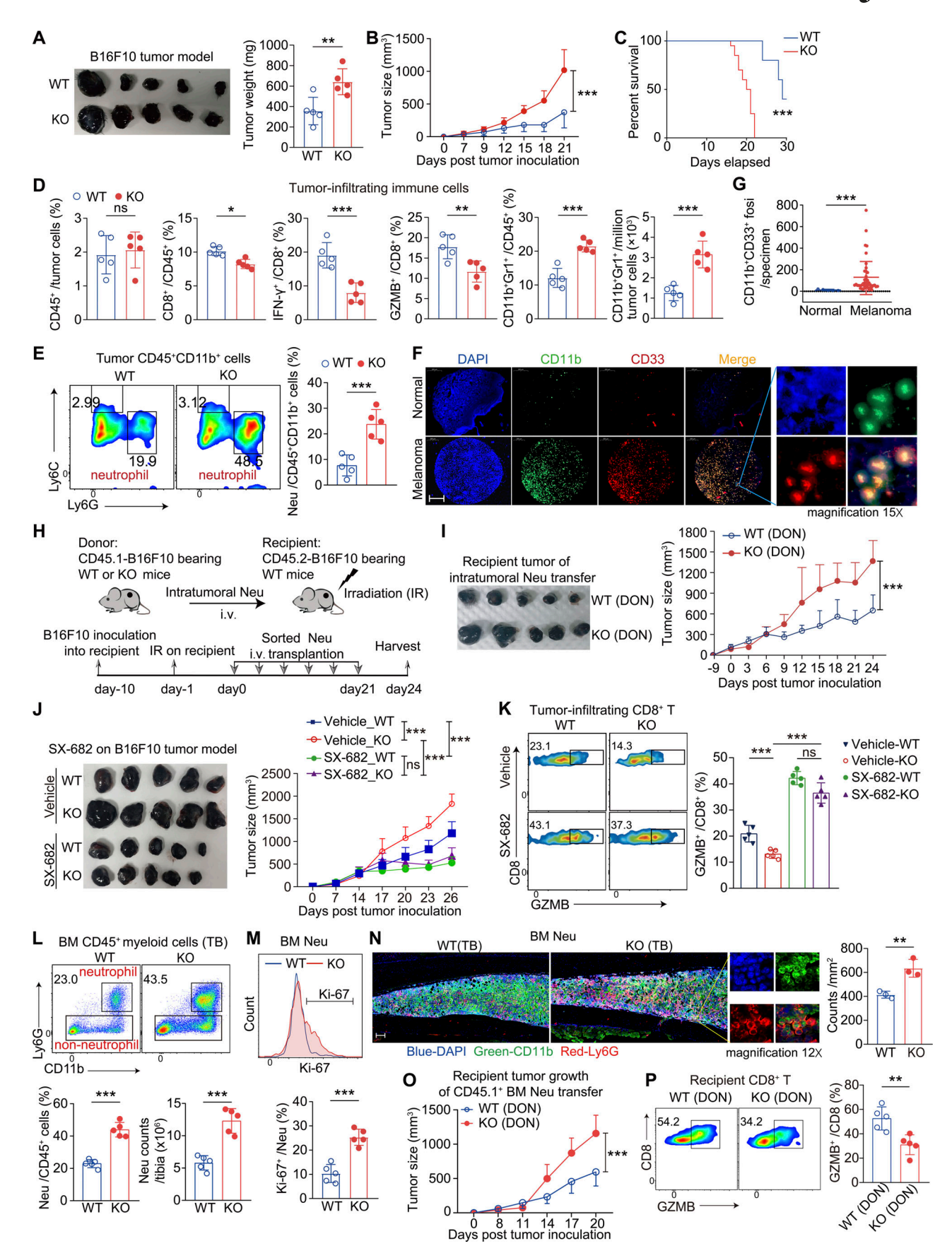


Figure 2. **MYO1F deficiency promoted tumor growth by inducing the expansion of TANs. (A)** Left: WT and $Myo1f^{-/-}$ C57BL/6 mice were subcutaneously injected with 2×10^5 B16F10 cells, tumor collection at day 21 (N = 5 in each group). Right: The corresponding tumor weight. **(B)** Tumor growth curve over time



of WT and $Myo1f^{-/-}$ C57BL/6 mice were subcutaneously injected with 2 × 10^5 B16F10 cells. (C) Kaplan–Meier survival curves of B16F10 tumor models described in A (N = 10 in each group). (D) FACS analyses of intratumoral CD45+, CD4+, CD8+ (IFN-y+ and GZMB+) cells, and neutrophils from tumor tissues described in A. (E) FACS analyses of intratumoral neutrophils from tumor tissues described in A. (F) Immunofluorescence staining of CD11b (green) and CD33 (red) in human melanoma (normal, N = 5; melanoma, N = 45). Scale bar: 200 μm. (G) Quantity statistics of colocalization in immunofluorescence staining (F). (H) Schematic of intratumoral neutrophil transfer from donor (CD45.1 B16F10 tumor-bearing WT or KO mice) to recipient (CD45.2 WT mice). (I) Tumor neutrophil transfer effect on tumor progression. Sorted neutrophils from donor tumor tissues of B16F10-bearing mice transfer into B16F10 tumor models of recipient. Left: Tumor collection on day 24 after subcutaneously injected with 2×10^5 B16F10 cells. Right: Tumor growth curve over time (N = 5 in each group). (J) SX-682 effect on B16F10 tumor models. Left: Tumor collection on day 26 after subcutaneously injected with 2×10^5 B16F10 cells. Right: Tumor growth curve over time (N = 5 in each group). Dose: 50 mg/kg, i.g., bid. (K) FACS analyses of intratumoral CD8+ (GZMB+) T cells (N = 5). (L) Top: Flow cytometry analyses of Ly6G and CD11b in BM CD45+ myeloid cells from WT and Myo1f-/- B16F10 models of day 21. Bottom: Statistic of neutrophil proportion and numbers by counting through FACS (N = 5). (M) Top: Flow cytometry analyses of Ki-67 in CD11b+Ly6G+ (Neu) clusters from BM of WT and Myo1f-/- B16F10 tumor models of day 21. Bottom: Statistic of Ki-67 proportion (N = 5). (N) Left: Representative immunofluorescence staining of CD11b (green) and Ly6G (red) in BM from WT and Myo1f-/-B16F10 model. Right: Statistic of neutrophil numbers by counting colocalization (N = 3). Scale bar: 500 µm. (O) BM neutrophil transfer effect on tumor growth curve over time. Sorted BM neutrophils from donor tumor tissues of B16F10-bearing mice of day 21 were transferred into B16F10 tumor models of recipient (N = 5). (P) FACS analyses of intratumoral CD8+ (GZMB+) T cells (N = 5). Data in A-E, H-M, O, and P represent one experiment of three independent repeats; F and N represent one experiment of two independent repeats. Data are presented as mean ± SD. P values were analyzed by one-way ANOVA test (B, I, I, and O); log-rank (Mantel-Cox) (C); two-tailed unpaired Student's t test (A, D, E, G, K-N, and P), *P < 0.05, **P < 0.01, and ***P < 0.001. ns, no significance. Neu, neutrophil.

Moreover, we detected a significant difference in the proliferative marker Ki-67 specifically in the BM-derived CD45+CD11b+Ly6G+ (neutrophil) populations but not in the CD45+Ly6G- (non-neutrophil) populations in KO mice (Fig. 2 M and Fig. S3 C). To validate this, the tibia was collected for immunofluorescence staining. Consistently, compared with those from WT mice, the BMs from KO tumor-bearing mice presented greater accumulation of the CD11b+Ly6G+ neutrophil populations (Fig. 2 N). Returning to the issue of neutrophil aggregation in tumors, we observed a similar trend of neutrophil expansion in the peripheral blood and spleen of KO mice (Fig. S3 D), which indicated that the massively expanded neutrophils infiltrated tumor tissues through the circulation, similar to the previously reported consensus. To define the role of BM neutrophils in tumor progression, this subset was sorted from tumor-bearing mice and transferred into myeloablative recipient tumor models (Fig. S3, E and F). Compared with the group of WT DON, the group treated with KO DON presented increased tumor growth (Fig. 2 O and Fig. S3 G) and decreased CD8⁺ T cell activation (Fig. 2 P).

Neutrophils contains huge amounts of S100A8 protein (one of the Ca²⁺-binding S100 protein family member) in the cytoplasm, which makes it a marker to target neutrophils (Pruenster et al., 2016). We used *Myo1f*^{flox/flox}-S100A8^{Cre} mice to consolidate the role of MYO1F in neutrophil during tumor progression. Importantly, we obtained results coincided with the total *Myo1f* KO mice regarding tumor growth (Fig. S3 H), survival rate (Fig. S3 I), neutrophil infiltration (Fig. S3 J), tumor-infiltrated CD8⁺ T cell activity (Fg. S3 K), and neutrophil aggregation in BM (Fig. S3, L and M).

Collectively, both mouse tumor models and human melanoma samples revealed a correlation between low level of MYO1F and extensive intratumoral neutrophils, which lead to an impaired anti-tumor immunity.

MYO1F deficiency enhances the immunosuppressive function of neutrophils and remodels the TME by inducing CTLs exhaustion

To determine the function of MYO1F in neutrophils, we sorted intratumoral neutrophils from B16F10 tumor-bearing WT and

KO mice (Fig. S2 D) and compared the gene expression profiles via RNA-sequencing (RNA-Seq) analysis (Fig. 3 A). Notably, neutrophils from KO mice presented high levels of *Cd274* (PD-L1), *Cxcl9* (CXCL9), *Nos2* (NOS2), *Cybb* (NOX2), *Arg1* (ARG1), *Il10* (IL-10), and *Ido1* (IDO1), indicative of an immunosuppressive potential of these MYO1F-deficient neutrophils. These genes were also verified via quantitative RT-PCR (RT-qPCR) (Fig. 3 B), which revealed a reshaped subset induced by MYO1F deficiency. While no significant change in the expression of *Icam1*, which was identified as the dominant regulator of neutrophil migration (Lyck and Enzmann, 2015), was consistent with that, MYO1F deficiency did not influence the migration ability in our study (Fig. S3 A).

Suppressions in immune response and inflammatory reaction are the prominent features of N2-like neutrophils, we then analyzed these two signaling base on the gene set enrichment analysis assay and found that the intratumoral neutrophils from KO mice exhibited markedly weaker activation for these pathways, further corroborating the role of MYO1F deficiency in promoting the immunosuppressive function of neutrophils (Fig. S3 N). Consistently, we found the high expression of Arg1 (Arg1), Ccl2 (CCL2), and Ccl5 (CCL5) in KO neutrophils, which are three classic markers (red color) for immunosuppressive N2-type neutrophils (Fig. 3 A). We then conducted co-culture assay of tumor-infiltrating neutrophils and CD8+ T cells. Besides the inhibition of proliferation, the exhaustion of T cells, identified by PD-1hi and TIM3+ signature of terminally exhausted T cells (Im et al., 2016; Paley et al., 2012; Wolf et al., 2020), was increased in KO neutrophil group (Fig. 3 C).

Interestingly, we analyzed the BM neutrophil transfer assay described in Fig. 2 O and found that the number of intratumoral CD45.1+ neutrophils in recipient of KO DON was >50% of WT DON (Fig. 3 D and Fig. S4 A), which was coincided with tumor neutrophil transfer assay in Fig. S2 K. We then detected apoptosis via annexin V and PI staining and found that the intratumoral CD45.1+ neutrophils in recipient of KO DON exhibited lower levels of late-stage apoptosis (annexin V+PI+) than those of WT DON at the endpoint of the experiment (Fig. 3 E and Fig. S4 B). To confirm this result, we detected the apoptosis in



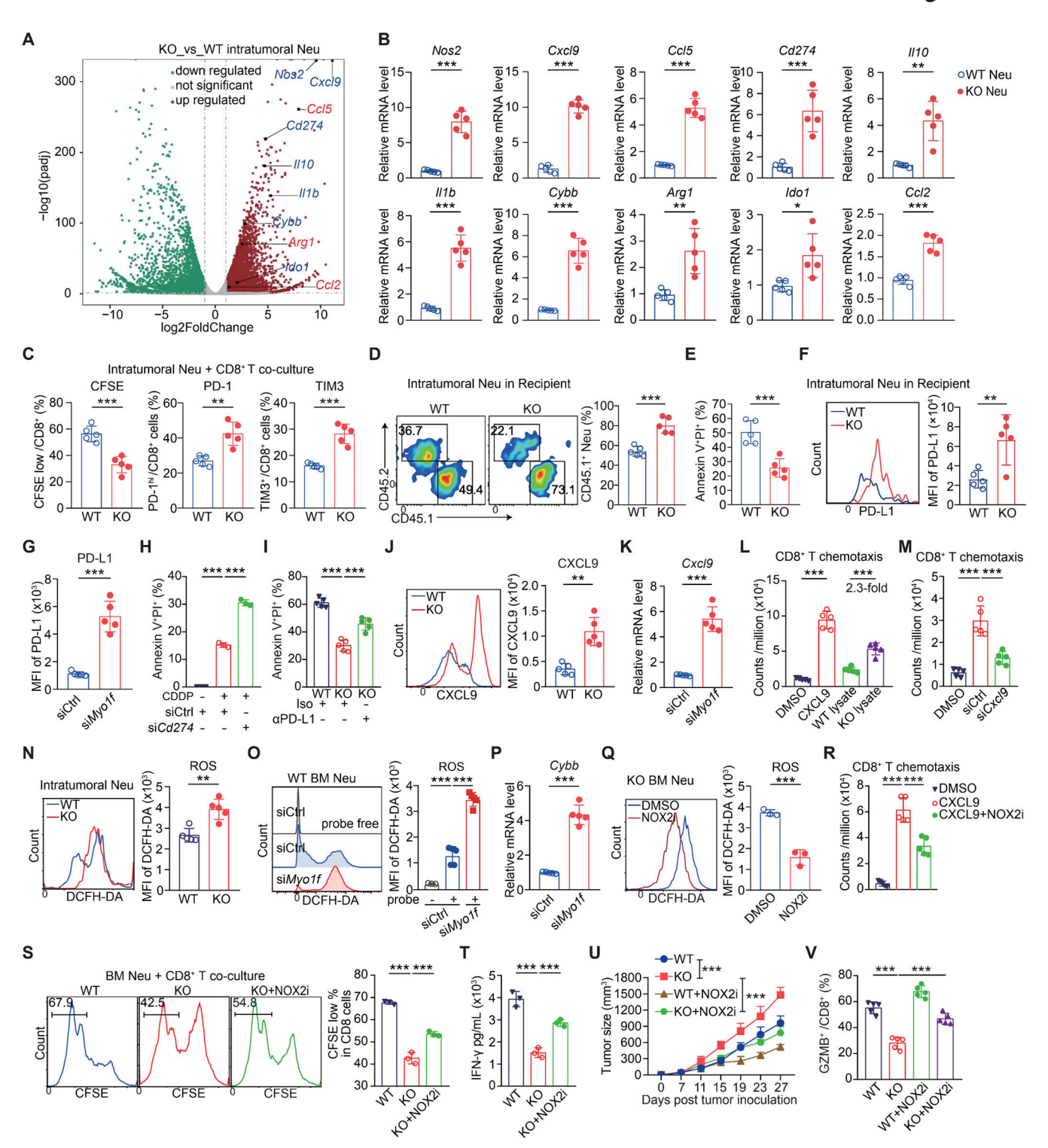


Figure 3. **MYO1F deficiency enhances the immunosuppressive function of TANs. (A)** Volcano plot of mRNA sequencing data of sorted tumor-infiltrating neutrophils from WT and $Myo1f^{-/-}$ B16F10 model. **(B)** Gene mRNA level was detected by RT-qPCR from sorted tumor-infiltrating neutrophils from WT and $Myo1f^{-/-}$ B16F10 model (N = 5). **(C)** FACS analyses of PD-1^{hi} and TIM3⁺ of CFSE-labeled CD8⁺ T cell co-culture with sorted tumor neutrophils from WT and $Myo1f^{-/-}$ B16F10 tumor models of day 21 (N = 5). **(D)** FACS analyses of recipient intratumoral CD45.1⁺ neutrophils in the BM neutrophil transfer tumor model as described in Fig. 2 O (N = 5). **(F)** FACS analyses of PD-L1 in intratumoral CD45.1⁺ neutrophils in recipient (N = 5). **(G)** Cultured neutrophils from WT mice were transfected with siCtrl, siMyo1f, and PD-L1 on neutrophils were analyzed 48 h after transfection by FACS (N = 5). **(H)** Cultured neutrophils from WT mice were transfected with siCtrl and siCd274; after 24 h, cells were treated with cisplatin at 1 μ M, and annexin V and PI staining were analyzed at 48 h after transfection by FACS (N = 3). **(I)** Cultured neutrophils from WT and Myo1f^{-/-} were incubated with anti-PD-L1 neutralizing antibody at 10 μ g/ml, and annexin V and PI staining were analyzed at 48 h after incubation by FACS (N = 5). **(K)** Cxcl9 mRNA levels were detected by RT-qPCR from cultured neutrophils treated with siCtrl or siMyo1f (N = 5).



(L) Chemotaxis assay of CD8+ T cell induced by cytokine and cell lysate. CD8+ T cell in the lower chamber counts by FACS with anti-CD8 flow staining with different treatment (N = 5). (M) Chemotaxis assay of CD8+ T cell induced by neutrophils. Cultured neutrophils from day 4 were transfected with siRNA or siCxcl9 for 24 h and set into the lower chamber with 3 × 10⁶ cells. Sorted CD8+ T cells were placed into the upper chamber of transwell set with 1 × 10⁶ cells. After 6 h, CD8+ T cell in the lower chamber counts by FACS with anti-CD8 flow staining with different treatment (N = 5). (N) FACS analyses of DCFH-DA-labeled tumor neutrophils from WT and $Myo1f^{-/-}$ B16F10 model of day 21 (N = 5). (O) FACS analyses of DCFH-DA-labeled cultured neutrophils from WT mice with transfections of siRNA of siCtrl or siMyo1f (N = 5). (P) Cybb mRNA levels were detected by RT-qPCR from cultured WT neutrophils treated with siCtrl or siMyo1f (N = 5). (Q) FACS analyses of DCFH-DA in cultured neutrophils from $Myo1f^{-/-}$ mice with treatment of NOX2i for 24 h (N = 5). (R) Chemotaxis assay of CD8+ T cell induced by cytokine and small molecular compound. CD8+ T cell in the lower chamber counts by FACS with anti-CD8 flow staining (N = 5). (S) FACS analyses of CFSE-labeled CD8+ T cell from BM neutrophil and CD8+ T cell co-culture assay (N = 3). (U) Cultured neutrophil transfer effect on tumor growth curve over time. Cultured neutrophils at day 5 treated with stattic (5 μ M) for 24 h before transfer (N = 5). (V) FACS analyses of intratumoral CD8+ (GZMB+) T cells described in U. Data in B-V represent one experiment of three independent repeats; A represents one experiment of two independent repeats. Data are presented as mean \pm SD. P values were analyzed by one-way ANOVA test (H, I, L, M, O, and R-V); two-tailed unpaired Student's t test (B-G, J, K, N, P, and Q); *P < 0.05, **P < 0.01, and ***P < 0.001.

intratumoral CD45.1+ neutrophils in recipient within 36 h after transfer and observed the late-stage apoptosis was also decreased in KO DON (Fig. S4 C). Recent studies revealed that high levels of PD-L1 could delay neutrophil apoptosis (Deng et al., 2021; Wang et al., 2021a). We found Cd274 (PD-L1) was highly expressed in KO neutrophils according to the RNA-Seq data, and this phenomenon was verified on intratumoral CD45.1+ neutrophils in recipients of KO DON (Fig. 3 F) and also on neutrophils in KO DON (Fig. S4 D). To determine the relationship between MYO1F and PD-L1, MYO1F was knocked down with siRNA (Fig. S4 E) in cultured BM neutrophils from TF WT mice, and the PD-L1 level subsequently increased (Fig. 3 G). To determine the effect of PD-L1 on neutrophil apoptosis in vitro, we detected apoptosis 24 h after the transfection of siRNA-Cd274 into cultured WT BM neutrophils followed by cisplatin (CDDP) induction and found that the number of apoptotic cells was greater in the siRNA-Cd274-transfected group than in the scramble control siRNA-transfected group (Fig. 3 H and Fig. S4 F) and that PD-L1 blockade decreased the apoptosis of neutrophils from KO mice (Fig. 3 I). Collectively, these data suggest that MYO1F deficiency could delay the apoptosis of neutrophils.

High expression levels of CXCL9 were detected at both transcriptional (Fig. 3, A and B) and protein levels in KO neutrophils (Fig. 3 J), and siRNA-Myolf significantly upregulated Cxcl9 (Fig. 3 K). Previous studies have shown that macrophages and DCs attract CD8+ T cell via high expression of CXCL9 (Chow et al., 2019), whereas the role of CXCL9 in N2-like neutrophils is not yet clear. Consistently, IL1b was increased in KO neutrophils (Fig. 3, A and B), which upregulated both Cxcl9 mRNA and stimulated the secretion of CXCL9 ligand (Guo et al., 2018). The upregulation of Cxcl9 was verified in cultured neutrophils (from WT tumor-free BM) treated with IL-1β (Fig. S4G). We speculated that a high level of CXCL9 could attract CD8+ T cell to neutrophils, leading to the exhaustion and apoptosis of T cells. We tested the chemotaxis of CD8+ T cell induced by either CXCL9 or neutrophils lysates with a transwell assay. Compared with WT neutrophils, KO neutrophils attracted 2.3-fold more CD8+ T cell into the lower chamber (Fig. 3 L) and that the knockdown of Cxcl9 with siRNA in cultured MYO1F-KO neutrophils abolished the chemotaxis of CD8+ T cell (Fig. 3 M). Furthermore, immunofluorescence staining was performed in tumor tissues of mice and co-culture of neutrophils and CD8+ T cells. Combination of neutrophils to CD8+ T cell in vivo was significantly increased in tumor tissues from Myolfff-S100A8Cre mice of B16F10 bearing

(Fig. S4, H and I). This trend of increasing binding ability was also validated in vitro by co-culture of KO neutrophils and CD8⁺ T cells (Fig. S4, J and K).

Next, we examined the factors that drive the reshaping of N2-like features in KO neutrophils. High expression of Cybb (NOX2) suggests the possibility of high ROS production, which was verified in tumor-infiltrating neutrophils (Fig. 3 N). This phenomenon was also observed in BM neutrophils of tumor model (Fig. S4 L), which indicated that the provenance of the ROS was from the BM. Since ROS are managed and feedback is from Nos2, Arg1, Il10, Cd274, and Ido1 expression (Ju et al., 2021; Vasquez-Dunddel et al., 2013), more work is needed to identify the driving factors involved. Neutrophils isolated from KO BM were pretreated with EUK-134, a superoxide dismutase mimic with catalase activity, and then stimulated with LPS to induce ROS (Fig. S4 M). Nos2, Illb, and IllO were mostly rescued to different degrees under EUK-134 treatment, unlike the other immunosuppressive factors, Cd274 (PD-L1) expression was not driven by ROS (Fig. S4 N). ROS are produced through NADPH oxidases (NOXs) (Prasad et al., 2017). Although Cybb (NOX2) expression is significantly increased in KO neutrophils, no direct evidence suggests that MYO1F regulates ROS production. To identify NOXs that determine high levels of ROS, MYO1F was knocked down with siRNA in cultured neutrophils (from WT tumor-free BM), which triggered ROS production (Fig. 3 O). The mRNA levels of NOXs were analyzed, and the NOX2 isoform was found to be significantly increased (Fig. 3 P and Fig. S4 O), which was consistent with the RNA-Seq data in Fig. 3 A. To validate the role of ROS induced by NOX2 in reshaping N2-like features, we used a NOX2 inhibitor (GSK2795039 and NOX2i) on cultured KO BM neutrophils and found that high levels of ROS could be rescued (Fig. 3 Q).

In addition, the chemotaxis of CD8 $^{+}$ T cell induced by KO neutrophils could be repressed by pretreatment with NOX2i (Fig. 3 R), which indicated that ROS were the driving factor leading to CD8 $^{+}$ T cell immune suppression. To further validate the effect of NOX2-induced ROS on the function of neutrophils, neutrophils were co-cultured with CD8 $^{+}$ T cell with or without NOX2i treatment. NOX2i-treated neutrophils from MY01F-KO mice presented decreased immunosuppressive ability based on proliferation (Fig. 3 S) and IFN- γ secretion (Fig. 3 T) by CD8 $^{+}$ T cell. We then transferred NOX2i-treated BM neutrophils into B16F10 models and found that, compared with no treatment, NOX2i treatment suppressed tumor growth (Fig. 3 U) and



rescued low GZMB production of intratumoral CD8⁺ T cell in KO adoptive receptors (Fig. 3 V and Fig. S4 P). Thus, the ROS production in MYO1F-deficient neutrophils was a crucial factor in shaping the N2-like features, and the new shaped subset remodeled the TME mainly by inducing CTLs exhaustion.

STAT3 activation is required for the proliferation and immunosuppressive function of TANs

Although the above findings indicate that ROS and PD-L1 regulated by MYO1F determine tumor progression and immunotherapy effects through neutrophils, the underlying signaling pathways are not yet clear. We analyzed the KEGG pathways associated with the RNA-Seq data and found enriched tendency in STAT3 activation pathway (Fig. S5 A). Moreover, we found that the phosphorylation of STAT3 was increased approximately threefold in BM neutrophils from KO tumor-bearing mice via FACS analysis (Fig. 4 A). We further used stattic, a classical inhibitor that blocks the STAT3 signaling pathway by preventing STAT3 phosphorylation (Fig. 4 B) (McMurray, 2006). Following treatment with stattic, the cultured KO neutrophils expansion capacity was markedly decreased in vitro, as indicated by the reduced Ki-67 level (Fig. 4 C).

Previous studies have shown that STAT3 signaling can promote NOX2 transcription and enhance ROS production (Condamine and Gabrilovich, 2011). Consistently, we found enhanced NOX2 transcription in MYO1F-knockdown neutrophils (Fig. 3 P), which further supports the assertion that MYO1F affects STAT3 signaling. Thus, we further used stattic to test the levels of ROS and NOX2 in cultured neutrophils from WT and KO mice and found that ROS production was repressed under stattic treatment condition (Fig. 4 D).

Besides, STAT3 activation induced PD-L1 expression in neutrophils from tumor-bearing mice and patients (Youn et al., 2008; Zhang et al., 2013). Importantly, the high PD-L1 level on KO neutrophils decreased after stattic treatment (Fig. 4 E). Both Cybb (NOX2) and CD274 (PD-L1) mRNA levels in KO BM neutrophils were decreased after stattic treatment (Fig. 4 F).

To verify the importance of STAT3 signaling in neutrophils immunosuppression triggered by MYOIF deficiency, we cocultured BM neutrophils from WT and KO tumor-bearing mice and CD8⁺ T cell in vitro and found that stattic treatment rescued CD8⁺ T cell activation (Fig. 4 G). To validate the effect of MYOIF-mediated STAT3 regulation on tumor progression, we transferred stattic-treated BM neutrophils into myeloablative tumor-bearing mice (Fig. 4 H). Interestingly, tumor growth was slower after the transplantation of stattic-treated neutrophils (Fig. 4 I and Fig. S5 B).

The above data demonstrated that both phenotype reshaping and expansion of neutrophils induced by MYO1F deficiency were dependent on the STAT3-ROS/PD-L1 signaling (Fig. 4 J).

MYO1F restrains STAT3 activation by inhibiting TRIM21mediated degradation of PHB1

We next sought to elucidate the molecular mechanism of MYO1F in regulating STAT3 signaling. To identify possible target proteins, we profiled previously published mass spectrometry data from MYO1F immunoprecipitates and identified TRIM21, an

E3 ubiquitin-protein ligase, as one of the top potential interactors (Sun et al., 2021). TRIM21 is a crucial trigger for STAT3 activation by binding to PHB1, which induces its ubiquitination and degradation (Alomari, 2021), and PHB1 acts as a tumor suppressor gene restraining cell proliferation by inhibiting STAT3 activity (Kathiria et al., 2012; Qureshi et al., 2015; Wang et al., 2019). We then performed confocal microscopy to confirm the colocalization of MYO1F with the TRIM21 protein in neutrophils (Fig. 5 A). Additionally, via pull-down experiments, we demonstrated the direct interaction of MYO1F with the TRIM21 protein both in neutrophils and in the 293T cell overexpression system (Fig. 5, B and C; and Fig. S5, C and D). Through the use of a variety of truncation/deletion designs and immunoprecipitation (IP) experiments, we revealed that the SH3 domain in the C terminus of MYO1F and the BBOX domain of TRIM21 are required for the protein interaction (Fig. 5, D-H).

TRIM21 is known to facilitate the ubiquitination of PHB1, which suppresses STAT3 phosphorylation (Kathiria et al., 2012; Qureshi et al., 2015; Wang et al., 2019). However, the binding ability of TRIM21/PHB1 is not constant, and in the presence of competitive binding partners, PHB1 is released to avoid degradation (Alomari, 2021). Interestingly, we discovered that MYO1F competitively interacted with TRIM21 to prevent its binding to PHB1 (Fig. 5 I). Moreover, we showed that this MYO1F/TRIM21 interaction directly suppressed the ubiquitination of PHB1 in vitro (Fig. 5 J). To confirm the role of PHB1 in STAT3 activity, we found STAT3 activity increased in neutrophils after the siRNA knockdown of Phb1 gene (Fig. 5 K). We further knocked down Myolf via siRNA, which led to a decrease in the PHB1 protein level (Fig. 5 L). To further verify the effect of MYO1F KO on PHB1 degradation, we performed ubiquitination detection in vitro and found an increase in the level of ubiquitination (Fig. 5 M). In conclusion, MYO1F restrained STAT3 activation by interacting with TRIM21 competitively, preventing PHB1 from ubiquitination and subsequent degradation (Fig. 5 N).

Tumor-derived TGF-β1 downregulates *Myo1f* expression in neutrophils

We applied MC38 tumor models in WT mice as a pathological condition to examine the dynamics of MYO1F level during tumor progression. We found the number of neutrophils in the BM increased after tumor inoculation (Fig. 6 A). Notably, we observed that the level of MYO1F decreased 1.5-fold in the neutrophil subset but not in the non-neutrophil subset from MC38 tumor-bearing mice (Fig. 6 B). We also detected MYO1F in neutrophils with the human melanoma array mentioned in Fig. 1 E and found that MYO1F level in neutrophils from normal tissues was higher than the nearby cells and decreased in melanoma (Fig. 6, C and D). Consistently, the MYO1F level detected by flow showed gradual reduction during tumor progression (Fig. 6 E).

To explore whether potential factors are derived from tumor cells, further in vitro treatment of neutrophils with conditioned media from various tumor cell lines revealed that MC38 and Hepal-6 cell supernatants reduced MY01F protein levels and suppressed *My01f* transcription in neutrophils (Fig. 6 F).

To identify the specific factor that affects *Myolf* gene expression, we examined the level of MYO1F after treatment with



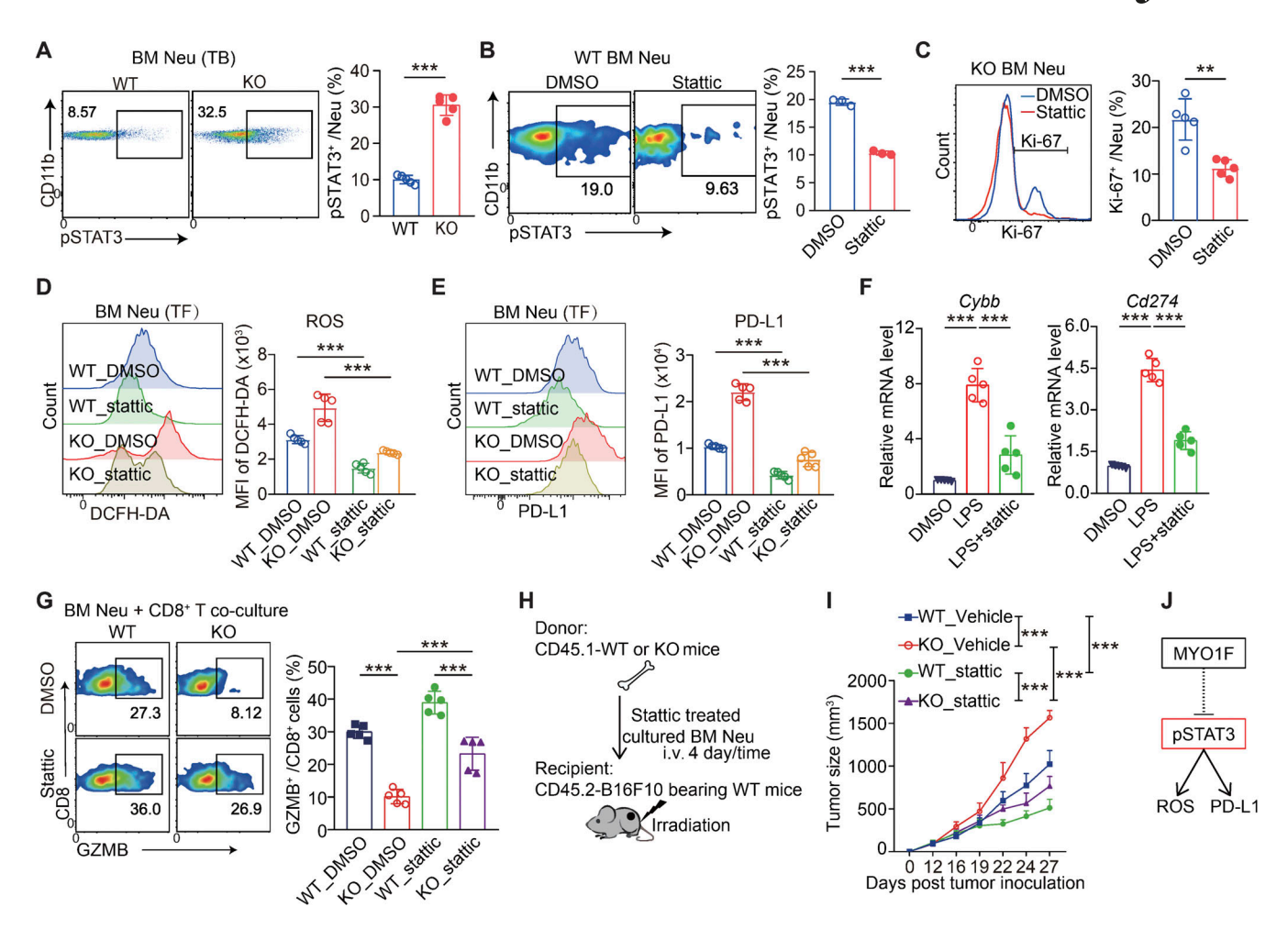


Figure 4. **Activation of STAT3 in neutrophils. (A)** FACS analyses of phosphorylated STAT3 on primary BM neutrophils from WT and $Myo1f^{-/-}$ B16F10 tumor models. **(B)** FACS analyses of phosphorylated STAT3 on cultured BM neutrophils from WT mice after 24 h of treatment with stattic (5 μ M, N = 3). **(C)** FACS analyses of Ki-67 on cultured neutrophils from WT BM after 5 days of treatment with stattic (5 μ M, N = 5). **(D)** FACS analyses of DCFH-DA-labeled BM neutrophils from WT and $Myo1f^{-/-}$ tumor-free model at day 5 after treated with stattic (5 μ M) for 24 h, (N = 5). **(E)** FACS analyses of PD-L1 on cultured BM neutrophils from WT and $Myo1f^{-/-}$ tumor-free model at day 5 after treated with stattic (5 μ M) for 24 h (N = 5). **(F)** Cybb and Cd274 mRNA level were detected by RT-qPCR on cultured BM neutrophils from WT and $Myo1f^{-/-}$ tumor-free model at day 5 after treated with stattic (5 μ M) for 24 h (N = 5). **(G)** FACS analyses of CD8+ (GZMB+) T cells from co-culture BM neutrophils from WT and $Myo1f^{-/-}$ tumor-free model treated with stattic (5 μ M) for 24 h (N = 5). **(H)** Schematic of cultured neutrophils with stattic (5 μ M) treatment transfer from donor (CD45.1 WT and KO mice) to recipient (CD45.2 B16F10 tumor-bearing mice). **(I)** Recipient tumor growth curve over time (N = 5). **(J)** Schematic diagram of MYO1F regulates ROS and PD-L1 by inhibiting STAT3 activation. Data in A-I represent one experiment of three independent repeats. Data are presented as mean \pm SD. P values were analyzed by one-way ANOVA test (D-G and I); two-tailed unpaired Student's t test (A-C); *P < 0.05, **P < 0.01, and ***P < 0.001. Neu, neutrophil; TB, tumor bearing; TF, tumor free.

various tumor-derived cytokines. Interestingly, we found that TGF- β 1 specifically decreased both MYO1F protein and mRNA levels in vitro (Fig. 6, G and H; and Fig. S5 E). Importantly, the induction of neutrophils expansion by tumor medium was also mimicked by TGF- β 1 treatment, as indicated by increases in Ki-67 expression (Fig. 6 I). We then treated neutrophils with a neutralizing antibody to reduce TGF- β 1 in the tumor medium supernatant, which resulted in reduced expansion (Fig. 6 J). To further validate the downregulation of MYO1F induced by TGF- β 1 from tumor cells described in Fig. 6 F, we approximated the TGF- β 1 levels in tumor cell lines via FACS and ELISA and found that MC38 and Hepa1-6 cells presented high levels of TGF- β 1 (Fig. S5 F). We next quantified TGF- β 1 secretion from tumor-infiltrating immune cells and detected comparable levels of TGF- β 1 in tumor cells and myeloid-derived cells (Fig. S5, G-I).

However, considering the extremely low proportion of immune cells in the TME (Fig. S5 J), the results indicated that TGF- β 1 was mostly derived from tumor cells.

To correlate the levels of TGF- β 1 and MYO1F in clinical conditions, the correlation analysis between the two factors with different tumor stages was profiled from the TCGA database. We found that increased TGF- β 1 expression with tumor progression correlated with a decreased MYO1F expression in 18 solid cancers (Fig. 6 K).

To further validate the effect of tumor-derived TGF- β 1 on neutrophils expansion, we generated a TGF- β 1 KO B16F10 cell line via CRISPR sgRNA-Tgfb1 (Fig. S5, K and L). Tumors with TGF- β 1 KO were inoculated into WT mice, and significantly fewer neutrophils were observed in the BM with the sgRNA-Tgfb1 than in the BM of the mice inoculated with the sgRNA-Ctrl



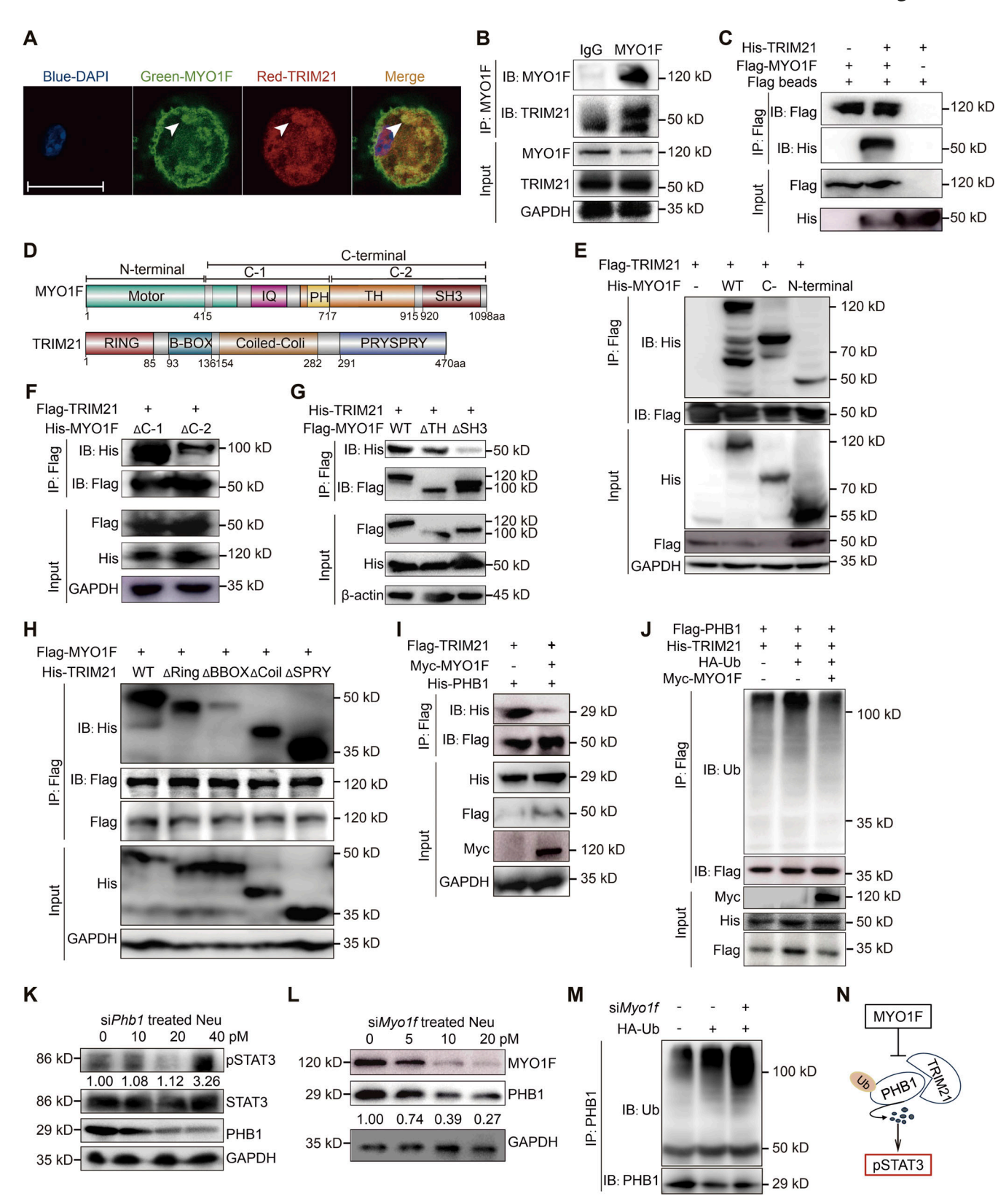


Figure 5. **MYO1F interacts with TRIM21 to prevent the ubiquitination and degradation of PHB1. (A)** Immunofluorescent staining of TRIM21 (red) and MYO1F (green) on neutrophils from WT BM obtained with laser modes and confocal fluorescence microscopy, DAPI used for cell nucleus indication. White arrowhead, colocalization of red and green colocalization (fosi). Scale bar: 50 μm. **(B)** Endogenous IP (co-IP) blot with BM neutrophils from WT mice, where IP was performed for MYO1F, and then precipitates were immunoblotted (IB) with an anti-TRIM21 antibody. **(C)** Exogenous co-IP blot with transfection of Flagtagged MYO1F and His-tagged TRIM21 in 293T, where IP was performed for Flag, and then IB with an anti-His antibody. **(D)** Schematic diagram of protein structure of MYO1F and TRIM21. **(E and F)** Specific combined domain to TRIM21 on MYO1F. Exogenous co-IP blot with transfection of Flag-tagged TRIM21 and



His-tagged truncated MYO1F in 293T, IP was performed for Flag, and then precipitates were IB with an anti-His antibody. (**G and H**) Specific combined domain to MYO1F on TRIM21. Exogenous Co-IP blot with transfection of Flag-tagged MYO1F and His-tagged TRIM21 in 293T, IP was performed for Flag, and then precipitates were IB with an anti-His. (**I**) MYO1F effect on TRIM21 and PHB1 binding ability. Exogenous co-IP blot with transfection of Flag-tagged TRIM21, Histagged PHB1, and Myc-tagged MYO1F in 293T, IP was performed for Flag, and then precipitates were IB with anti-His and anti-Myc antibodies. (**J**) MYO1F effect on exogenous PHB1 ubiquitination. Exogenous co-IP blot with transfection of Flag-tagged PHB1, His-tagged TRIM21, Myc-tagged MYO1F, and HA-tagged ubiquitin in 293T, IP was performed for Flag, and then precipitates were IB with anti-ubiquitin antibody. (**K**) Cultured neutrophils from WT mice were transfected with si*Phb1*, and MYO1F protein levels were analyzed 48 h after transfection by immunoblotting. (**L**) Cultured neutrophils from WT mice were transfected with increased siMyo1f (0, 5, 10, and 20 pM); MYO1F and PHB1 protein levels were analyzed 48 h after transfection by immunoblotting. (**M**) MYO1F effect on endogenous PHB1 ubiquitination. Cultured neutrophils from WT mice were transfected with si*Myo1*f 20 pM, and PHB1 was immunoprecipitated with corresponding antibody and IB with anti-ubiquitin antibody. (**N**) Schematic diagram of MYO1F regulates STAT3 activation by interacting with TRIM21 and protecting PHB1 from degradation. Data in A–M represent one experiment of three independent repeats. Source data are available for this figure: SourceData F5

tumors (Fig. 6 L and Fig. S5 M). The MYO1F expression level was also restored to a level comparable with that in tumor-free mice (Fig. 6 M). Moreover, decreased TGF- β 1 levels in both blood and BM were observed in mice inoculated with TGF- β 1 KO tumor cells, which demonstrated the direct impact of tumor-derived TGF- β 1 on neutrophils in the BM through the circulation (Fig. 6 N). Notably, TGF- β 1 signaling could lead to STAT3 activation by multiple downstream activities (Calon et al., 2012). Interestingly, we found a decrease of STAT3 activation under condition of MYO1F overexpression in cultured neutrophils (Fig. S5 N) and a significant increase under MYO1F deficiency condition (Fig. S5 O). Thus, tumor-derived TGF- β 1 regulates STAT3 activity by modulating the level of MYO1F in neutrophils.

TGF-β1 regulated *Myo1f* expression by promoting CpG methylation of SPI1-binding region in the intron 8

Determining the mechanism underlying the TGF-β1-mediated regulation of MYO1F expression in neutrophils is urgent. We first predicted possible transcription factors of the Myolf gene via analysis of the JASPAR database (Castro-Mondragon et al., 2022). Interestingly, we found that SPII has the potential to bind to multiple introns within the Myolf locus (Fig. S5 P). We further analyzed the expression patterns of MYO1F and SPI1 in clinical cancer specimens via the GEPIA2 and detected a strong correlation between the expression of the MYOIF and SPII genes but not between the expression of the MYO1E and SPI1 genes (Fig. 7 A). SPI1 is a member of the ETS domain transcription factor family, which is critical for myeloid and lymphoid lineage commitment and maturation (Olson et al., 1995). We next conducted siRNA experiments on neutrophils and found that Spi1 knockdown induced significant downregulation of MYO1F at both the transcript and protein levels (Fig. 7, B and C).

We analyzed SPI1 chromatin immunoprecipitation sequencing (ChIP-Seq) data from the Cistrome database (Wang et al., 2014) and found that SPI1 was bound to multiple sites within the *MyoIf* gene locus in different immune cells (Fig. 7 D) (Bornstein et al., 2014; Calero-Nieto et al., 2014; Carey et al., 2018; Eichenfield et al., 2016; Humblin et al., 2017; Ochiai et al., 2013). Notably, most binding peaks were distributed in introns, and no obvious binding peaks on the classical promoter region (–2 kb to the TSS), which is consistent with the binding sites predicted by JASPAR (Fig. S5 P). Importantly, SPI1 specifically bound to intron 8 of *MyoIf* in cells of the myeloid lineage, including BM myeloid cells, DCs, and macrophages, whereas no binding was

detected in cells of the lymphoid lineage (Fig. 7 D). Moreover, this binding pattern of SPI1 to intron 8 was correlated with high MYO1F protein levels in myeloid cell types (Fig. 7 E) and with high mRNA level in sorted immune neutrophils (Fig. S5 Q) from tumor-free mice spleen, which also indicated MYO1F was specifically highly expressed in neutrophils.

Recent advances have shown that introns can significantly increase gene expression by acting as internal promoters (Nott et al., 2003). Thus, we cloned the 400-bp segment containing the ChIP-binding peaks of SPI1 in different regions (-4 kb; introns 1, 8, and 21; 3' UTRs) into a pGL3 vector to examine the promoter activity via a dual-luciferase reporter assay. Surprisingly, the 400-bp segment of intron 8 showed strong promoter activity (Fig. 7 F). We predicted intron 8 in its entirety via Softberry; notably, the conserved segment overlapped with the SPI1-binding potential, and the predicted TATA box and promotor implied potential promoter activity for intron 8 (Fig. S5 R). Collectively, these data indicate that the binding of SPI1 to intron 8 of *Myo1f* is the key to promote transcription of *Myo1f*.

We next explored the core-binding site of SPI1 on intron 8. Notably, the 100-bp core peak sequence (two flanking of the SPI1-ChIP peak) within the 400-bp segment of intron 8 contained a conserved 10-bp SPI1-binding motif (MA0079.2) on the reverse strand (Fig. 7 G). Importantly, the luciferase assay revealed that deletions of either the 100-bp core peak or the 10-bp SPI1-binding motif abolished promoter activity compared with the 400-bp segment of intron 8 (Fig. 7 H). The above data suggested that SPI1 promotes *Myo1f* gene expression by specifically binding to intron 8 of the *Myo1f* gene.

Recent research has suggested that the binding capacity of SPI1 to targeted promoters could be regulated by TGF- β 1 (Heinz et al., 2006; Jurkin et al., 2010). We found that treatment of neutrophils with TGF- β 1 attenuated the promoter activity of intron 8, as observed in the luciferase assays (Fig. 7 I), which indicated the decreased binding capacity of SPI1 to intron 8. We then used ChIP-RT-qPCR to validate this finding and found that the segment (100-bp core peak) binding to SPI was significantly reduced after TGF- β 1 treatment (Fig. 7 J).

To investigate whether DNA methylation is induced by TGF- β 1, we performed bisulfite sequencing PCR (BSP) on intron 8 of MyoIf in TGF- β 1-treated neutrophils. Interestingly, the CpG methylation at position #2 increased 42% under TGF- β 1 treatment, whereas methylation at the other CpG positions did not significantly change (Fig. 7 K). Notably, CpG #2 is located only



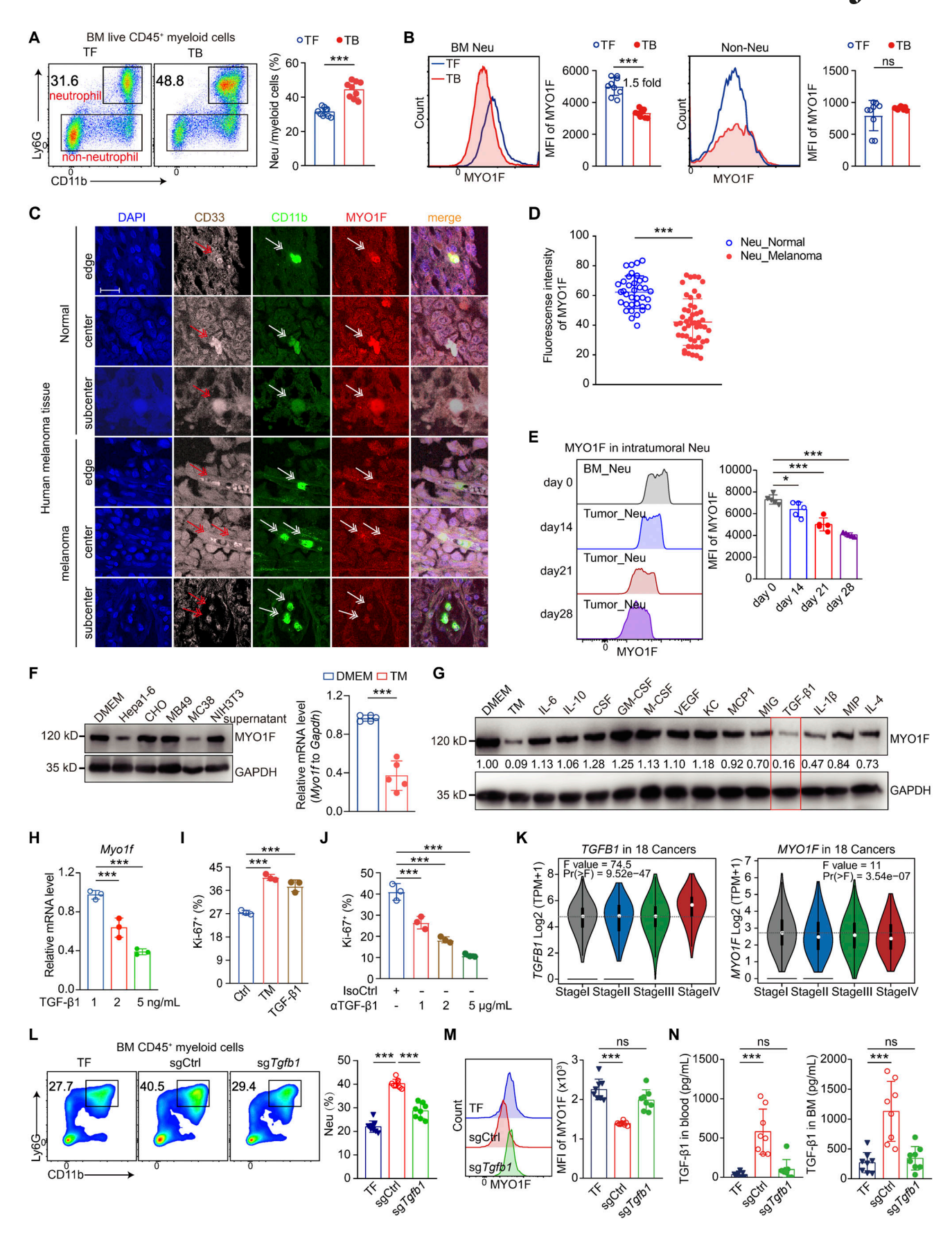


Figure 6. **TGF-\beta1 induces downregulation of MYO1F level in neutrophils. (A)** FACS analyses of CD11b+Ly6G+ neutrophils in primary BM from MC38 tumor-free and MC38 tumor-bearing models (N = 9). **(B)** FACS analyses of MYO1F on neutrophils and non-neutrophils in primary BM from tumor-free and



MC38 tumor-bearing models (N = 9). (C) Representative fluorescence staining of neutrophils infiltration in human melanoma (blue, DAPI; grayish white, CD33; red, MYO1F), 30 (normal) and 50 (melanoma) representative images for each group were counted. Scale bar: 50 μm. (D) Statistical analyses of fluorescence intensity of MYO1F in neutrophils, Neu_Normal, N = 30; Neu_Melanoma, N = 50. (E) FACS analyses of MYO1F level by staining with fluorescent antibodytargeting MYO1F on BM neutrophils and tumor-infiltrating neutrophils at different time (N = 5). (F) Cultured neutrophils were treated with supernatant from cell lines; MYO1F protein levels were analyzed 72 h after treatment by immunoblotting. Myo1f mRNA levels were detected by RT-qPCR from cultured neutrophils treated with mixture supernatant from MC38 and Hepa1-6 cell lines (N = 5). TM: mixture supernatant from MC38 and Hepa1-6 cell lines. (G) Cultures neutrophils were treated with indicated commercial cytokines; MYO1F protein levels were analyzed 48 h after treatment by immunoblotting. TM: mixture supernatant from MC38 and Hepa1-6 cell lines was used as positive control. (H) Cultured neutrophils were treated with TGF-β1 (1, 2, and 5 ng/ml); Myo1f mRNA levels were detected by RT-qPCR (N = 3). (I) Neutrophils at day 2 treated with medium, TM, and TGF- β 1 (5 ng/ml); Ki-67 was detected as proliferation marker by FACS 96 h after TGF- β 1 treatment (N = 3). (J) Anti-TGF- β 1 (0, 1, 2, and 5 μ g/ml) used in TM-cultured neutrophils to neutralize supernumerary TGFβ1 in microenvironment; Ki-67 was detected as proliferation marker by FACS 96 h after anti-TGF-β1 treatment; isotype control antibody used as control; TM: mixture supernatant from MC38 and Hepa1-6 cell lines. (K) Violin plots of TGFB1 and MYO1F gene expression in tumor stages of 18 cancers: ACC, CESC, cholangio carcinoma (CHOL), COAD, glioblastoma multiforme (GBM), head and neck squamous carcinoma (HNSC), KICH, kidney renal papillary cell carcinoma (KIRP), acute myeloid leukemia (LAML), brain lower grade glioma (LGG), LIHC, LUAD, OV, sarcoma (SARC), testicular germ cell tumors (TGCT), THCA, THYM, and UCEC. (L) FACS analyses of CD11b+Ly6G+ neutrophils in BM CD45+ myeloid cells from sgRNA-transfected B16F10 models, tumor-free mice. (M) FACS analyses of MYO1F protein level on CD11b+Ly6G+ neutrophils. (N) ELISA detection of TGF-β1 level from peripheral blood serum (dilution in 400 μl RPMI1640 of 100 μl serum) and extract of total BM (dilution in 500 μl RPMI1640 of a tibia). Data in A, B, F-I, and L-N represent one experiment of three independent repeats; C-E represent one experiment of two independent repeats. Data are presented as mean ± SD. P values were analyzed by one-way ANOVA test (E and H-N); two-tailed unpaired Student's t test (A, B, D, and F), *P < 0.05, **P < 0.01, and ***P < 0.001. ns, no significance; TM, tumor medium; TF, tumor free; TB, tumor bearing. Source data are available for this figure: SourceData F6.

1 bp away from the SPI1-binding site (Fig. 7 K). Moreover, replacement of the mutant CpG #2 site with adenine reversed the suppression of promoter activation induced by TGF- β 1 treatment (Fig. 7 L), which indicated that CpG #2 is the main site at which TGF- β 1 induces DNA methylation to prevent the binding of SPI1.

Discussion

Previous studies have identified N2 phenotype TANs cause ICB resistance, revealing the molecular mechanism underlying the function and proliferation of TANs is critical for improving the efficacy of immunotherapy. Our study revealed that MYOIF plays a key role in suppressing neutrophil expansion and toward N2-like phenotype transforming, providing valuable insights into indicators of ICB efficacy.

TGF- β 1 within the TME is considered the trigger for reshaping the N2 protumor phenotype (Fridlender et al., 2009). However, the specific underlying mechanism is still not clear. Of note, both immunosuppressive N2 TANs and TGF- β 1 are critical factors in determining ICB response, either dependent or independent. In this study, we connected these two factors at the molecular level by revealing the MYO1F as the regulatory hub.

MYO1F has been proposed in myeloid proliferation during tumor progression (Diquigiovanni et al., 2018; Duhoux et al., 2011; Taki et al., 2005) and remodeling immunological characteristics of neutrophils (Kim et al., 2006). We found that MYO1F is downregulated in human cancers and shows an unfavorable correlation with patient survival. Moreover, our data demonstrated TGF- β 1 can specifically downregulate *Myo1f* expression in neutrophils and reshape them into N2-like neutrophils.

Abnormal DNA methylation patterns lead to differential gene expression, and TGF- β 1-induced DNA methylation plays an important role in the occurrence and development of tumors (Matsumura et al., 2011; Zhang et al., 2011). Our work demonstrated that the regulatory mechanism of MYO1F expression in neutrophils is that the binding ability of SPI1 to *Myo1f* eighth intron, which acting as the internal promoter of *Myo1f* gene, was

inhibited by TGF- β 1-induced DNA methylation of neighboring site. Consistently, we found that the binding of SPI1 to the eighth intron of *MyoIf* is specific in myeloid cells but not in lymphoid cells based on the current CHIPseq database of Cistrome.

STAT3 is a critical regulator in reshaping immunological characteristics of TANs (Bitsch et al., 2022; Wang et al., 2023). The activation of STAT3 is influenced by ubiquitin ligases and deubiquitinating enzymes, which affect upstream regulatory factors (Lin et al., 2021; Sarri et al., 2022). Here, we identified TRIM21 as the specific E3 ligase determining STAT3 activation in MY01F pathway. Interestingly, TGF- β 1 is also the effective signal to induce the activation of STAT3 (Calon et al., 2012; Tang et al., 2017). Thus, we discovered the whole pathway of TGF- β 1/MY01F/STAT3, providing a new direction for investigating the functional mechanism of TANs.

ROS-related metabolic reprogramming underpins the reshaping of immunosuppressive ability and chemotaxis of TANs (Araźna et al., 2015; Correale, 2021; Fossati et al., 2003; Ju et al., 2021; Kelly et al., 2010). ROS does not function alone, and the mutual regulatory effects of ROS with NOS2, ARG1, IL-10, IDO1, etc., together contribute to the potent immunosuppressive ability of TANs (Chen et al., 2012; Hegde et al., 2021; Holokai et al., 2020). In this study, we found that the high level of ROS induced by MYO1F deficiency played a dominant role in shaping neutrophils into an N2-like protumor phenotype.

It is worth noting that the disability of CD8⁺ T cell is an important event in the TME leading to the resistance to ICB therapies (Budimir et al., 2022; Dolina et al., 2021; Kang et al., 2024). N2 neutrophils were proved to decrease the activation status of CD8⁺ T cell (Fridlender et al., 2009). Previous studies have suggested pro-inflammatory N1 neutrophils could attract and activate CD8⁺ T cell by producing pro-inflammatory cytokines (Scapini et al., 2000). N2 neutrophils do not produce high levels of such pro-inflammatory agents, and the interaction pattern of N2 neutrophils with CD8⁺ T cell is unclear. Here, we demonstrated that N2 neutrophils induced by MYO1F deficiency could also attract CD8⁺ T cell with in vitro chemotaxis assay and in vivo visualization validation in tumor tissues by



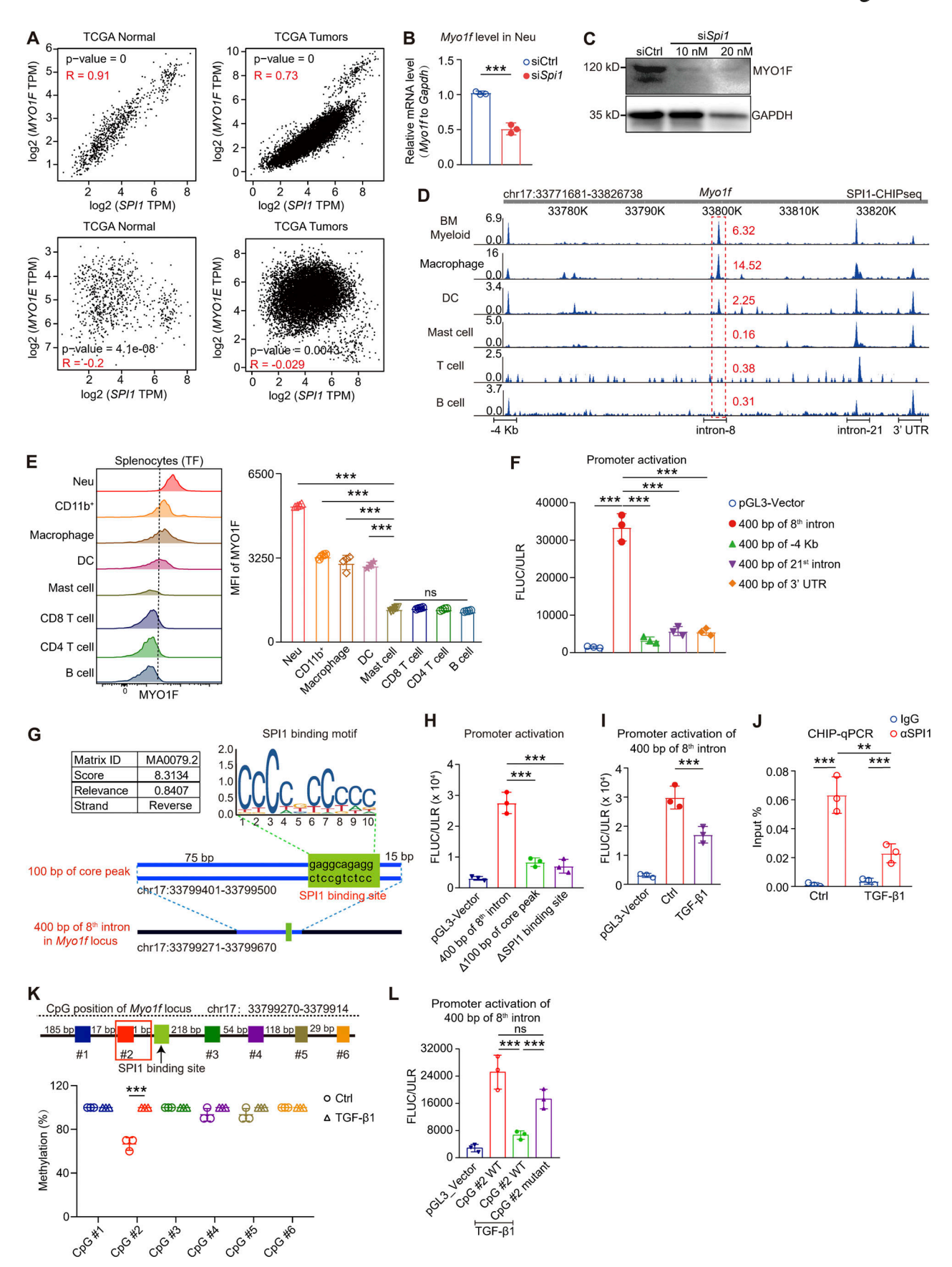


Figure 7. **TGF-β1 promotes CpG methylation in the intron 8 of Myo1f locus to inhibit SPI1 binding. (A)** Correlation analysis of SPI1 and MYO1F/MYO1E, using expression datasets from the TCGA database via the GEPIA2 website. **(B)** Myo1f mRNA levels were detected by RT-qPCR from cultured neutrophils 48 h



after transfection of siSpi1 (N = 3). (C) MYO1F protein levels were analyzed 72 h after transfection of siSpi1. (D) Murine SPI1-CHIP-Seq peak plot on chr17: 33771681–33826738. References are described in the main text. (E) FACS analyses of MYO1F on immune cells from WT mice (N = 5). (F) The transcription activity of 400-bp segment included each peak, measured by using a pGL3 vector luciferase reporter gene assay, after transfection into cultured neutrophils. (G) Schematic of SPI1-binding segment located on eighth intron. (H) The transcription activity of full-length and SPI1-binding truncated eighth intron measured by using a pGL3 vector luciferase reporter gene assay after 48 h of transfection into cultured neutrophils. (I) The transcription activity of 400-bp SPI1-binding segment 36 h after TGF- β 1 5 ng/ml treatment. (J) ChIP-RT-qPCR on enriched DNA IP by anti-SPI1 pulldown; IgG was used as control. (K) Top: Schematic of CpG methylation distributed in eighth intron of chr17: 33799270–3379914. Bottom: Evaluation of CpG methylation by BSP sequencing. (L) The transcription activity of WT (CpG#2 mutant) and adenine-replaced mutant (CpG #2 mutant) of 400-bp SPI1-binding segment, 48 h after TGF- β 15 ng/ml treatment. Data in B, C, E, F, and H–L represent one experiment of three independent repeats. Data are presented as mean \pm SD. P values were analyzed by one-way ANOVA test (E, F, H–J, and L); two-tailed unpaired Student's t test (B), *P < 0.05, **P < 0.01, and ***P < 0.001. ns, no significance. Neu, neutrophil. Source data are available for this figure: SourceData F7.

overexpression of CXCL9. This establishes that MYO1F deficiency in neutrophils is an important factor in remodeling the TME by inducing the exhaustion of T cells efficiently.

As the expression level of MHC-I on tumor is a key element in immunogenicity that related with ICB response (Gu et al., 2021). B16F10 tumor model was recognized as an immunologically "cold" tumor that typically exhibits moderate responsiveness to ICB (Francis et al., 2020). Though with moderate MHC-I expression and ICB responsiveness, this mouse melanoma model can mimic the characteristics of human melanoma in terms of histopathology and molecular arrangement, which is helpful for studying the pathogenesis of human melanoma and the functions of TILs. Thus, B16F10 was used in animal model for ICB therapies (Chin et al., 2021; Francis et al., 2020; Xun et al., 2024; Zhou et al., 2024). Moreover, by conducting experiments in both B16F10 and MC38 tumor models with distinct characteristics under Myolf KO conditions, we have demonstrated the critical role of the TGF-β1-MYO1F axis in modulating immune responses in both conditions.

In conclusion, our study revealed that TGF- β 1-induced downregulation of MYO1F in neutrophils could promote the immunosuppressive ability and expansion via the STAT3-ROS/PD-L1 signaling pathways. This work provides valuable insights into indicators of ICB efficacy and prognosis. We acknowledge the limitations of our study, which primarily used mouse tumor models, and further validation is needed to confirm the applicability of our findings to human tumors. Further investigation of MYO1F-STAT3-ROS/PD-L1 pathway is needed to plot the detailed reprogramming map of N2-like neutrophils in vivo.

Materials and methods

Study design

The primary aims of this study were to (1) characterize a crucial factor regulating neutrophils involved in ICB resistance, (2) identify the molecular mechanism underlying regulation of neutrophils, and (3) investigate the pathological regulation mechanism of crucial factor in neutrophils. We first profiled gene expression in clinical cancers and ICB cases and identified MYO1F as a key factor. We then used a combination of research methods in MYO1F KO mice, including RNA-Seq, B16F1O, and MC38 tumor models; adoptive transfer models; flow cytometry; and basic molecular biochemical techniques. Through tumor models on gene KO mice, MYO1F was confirmed as the crucial factor in suppressing tumor progression by restraining

neutrophils accumulation. Through adoptive transfer experiments, we demonstrated that the immunosuppressive ability, apoptosis, and proliferation of neutrophils were reshaped mediated by MYO1F deficiency. RNA-Seq was then performed and identified the driven genes and potent signaling pathway underlying in reshaping neutrophils. Last, through the co-culture of tumor cell lines supernatant and cytokines with neutrophils, it was finally confirmed that TGF- β 1 is the key factor regulating MYO1F expression in the pathological environment. In the end, the specific molecular mechanism of TGF- β 1–regulating MYO1F was identified through methylation sequencing and ChIP-RT-qPCR by combining CHIP-Seq data from Cistrome database. Experiments in this study were conducted at least three times unless otherwise specified in the figure legends.

Mice

C57BL/6J WT and Myo1f-/- mice and B6.SJL-Ptprca Pepcb/BoyJ (CD45.1) (stock number 002014) mice were purchased from The Jackson Laboratory. CD45.1-tagged WT and Myolf-/- mice were generated by hybridizing C57BL/6J WT Myolf-/- with CD45.1 mice, and homozygotes were obtained by inbreeding of filial generation at least two generations for homozygotes. Myolf flox/fox mice and S100A8cre mice were generously provided by Dr. Chenhui Wang, The Key Laboratory for Human Disease Gene Study of Sichuan Province and the Department of Laboratory Medicine, Sichuan Provincial People's Hospital, University of Electronic Science and Technology of China, Chengdu, China (Wang et al., 2025) and Dr. Jing Wang, Shanghai Institute of Immunology, Department of Immunology and Microbiology, State Key Laboratory of Oncogenes and Related Genes, Shanghai Jiao Tong University School of Medicine, Shanghai, China (Miao et al., 2023), respectively. Myolf flox/fox-S100A8cre mice were generated by hybridizing the two strains at least two generations for homozygotes. All the mice were housed under specific pathogen-free conditions, and the experimental protocols were approved by the Institutional Animal Care and Use Committee of the Shanghai Jiao Tong University School of Medicine.

Cell lines

293T, B16F10, MC38, Hepa1-6, NIH3T3, CHO, and MB49 cells were maintained in Dulbecco's modified Eagle's medium plus 10% FBS and 1% penicillin-streptomycin. 4T1 were maintained in RPMI-1640 medium plus 10% FBS and 1% penicillin-streptomycin.



Generation of neutrophils from murine BM in vitro

The generation of neutrophils in vitro was performed as previously described (Eckert et al., 2021). Briefly, CD11b+Ly6G+ cells were sorted from healthy C57BL/6 mice BM with Neutrophil Isolation Kit (Miltenyi Biotec) according to the manufacturer's manual. 2.5 \times 106 sorted cells were cultured in a 10-cm cell culture dish (Corning FALCON) in 10 ml RPMI-1640 medium with GlutaMAX supplemented with 10% heat-inactivated FBS, 1% penicillin/streptomycin, 10 mM Hepes buffer, 1 mM sodium pyruvate, 50 μ M β -mercaptoethanol, 1 mM MEM nonessential amino acids (all Thermo Fisher Scientific), 40 ng/ml GM-CSF (PeproTech), and 40 ng/ml IL-6 (PeproTech) for 6 days. In this study, most in vitro cell experiments start at day 4 if there is no special indication.

Neutrophil transplant

For tumor-infiltrating neutrophil transplantation. C57BL/6 (CD45.2+) recipient mice were subjected to subcutaneous inoculation of B16F10 on its back 10 days before. Tumor same-sized mice (~150 mm³) were chosen for conditional irradiation (950 rad) with a lead shielding chamber to protect tumor from irradiation. The tumor-infiltrating neutrophils in donor were sorted by aseptic flow cytometry from tumor tissues of WT (CD45.1+) and Myolf^{-/-} (CD45.1⁺) mice at day 21 after B16F10 inoculation. Briefly, first enrich the lymphocytes by percoll and stain with live and dead dyes followed by subsequent anti-CD11b (PE) and Ly6G (APC) staining. CD11b+Ly6G+ population was sorted by BD FACS Calibur for subsequent transplant. The flow sorting was performed depending on injecting time points. 2 × 106 tumorinfiltrating neutrophils were i.v. injected every 4 days into each irradiated recipient. Tumor was harvested 24 days after first injection.

ROS assay

Cultured neutrophils were preloaded with 10 μM DCFH-DA for 30 min in the dark. Probe was washed and incubated in probefree medium for another 10 min. FACS was used to detect the degree of probe loading with FITC channel.

Western blot

Tissues or cell lysates were prepared for western blot analysis with the following antibodies: MYO1F (sc-376534; Santa Cruz), TRIM21 (A13547; ABclonal), PHB1 (2426S; CST), STAT3 (9132; CST), pSTAT3 (9145; CST), His-tag antibody (12698; CST), Flagtag antibody (14793; CST), and GAPDH (9145; CST). ANTI-FLAG M2 Affinity Gel (A2220-1ML; Sigma-Aldrich).

Immunofluorescence

For MYO1F and TRIM21 colocalization, 1×10^5 cultured neutrophils from day 4 were seeded onto a 35-mm glass slide in the form of cell suspension and cultivated in a CO_2 incubator for another 6 h. The adherent cells were washed with PBS and fixed with 4% paraformaldehyde subsequently. After permeabilization with 0.5% Triton X-100 for 15 min at room temperature, cells were incubated with 1% BSA and then incubated with primary antibodies overnight at 4°C (MYO1F, sc-376534; Santa Cruz; TRIM21, A13547; ABclonal) and detected with goat anti-

mouse Alexa 488(1:1,000; Abcam), goat anti-rabbit Alexa 647 (1:1,000; Abcam), and DAPI (1:1,000; Thermo Fisher Scientific). Images were acquired with Leica SP8 laser confocal microscope and further analyzed with ImageJ software.

For neutrophil imaging in bone, tibias were freshly isolated from euthanized mice and decalcified in 10% EDTA for 3 days at room temperature. Tibias were cryopreserved in 30% sucrose for 48 h at 4°C, followed by embedding in a 50% O.C.T. (Tissue-Tek) and 50% (30%) sucrose mixture in a liquid nitrogen bath. Bones were then sectioned into 12- μ M slices at longitudinal axis, and the slices with most contents were chosen on slides for next step. Slides were incubated with goat serum plus 0.1% Triton X-100 for 30 min at room temperature, then incubated with primary antibodies overnight at 4°C (CD11b, ab8878; Abcam; Ly6G, A22270; ABclonal) and detected with goat anti-Rat IgG (1:1,000; Abcam), goat antirabbit IgG (1:1,000; Abcam), and DAPI (1:1,000; Thermo Fisher Scientific).

For neutrophils in mice tumor and human melanoma cancer tissue microarray (YP-MME1002c, YEPCOMEBio), multiplex immunofluorescence staining procedure on paraffin-embedded tissue section was followed by the instruction of supplier (cat. no. abs50013; Absin) and blocked with TBST containing 5% goat serum before incubation with antibodies (CD11b, ab8878; Abcam; Ly6G, A22270; ABclonal; CD8, abs120101; Absin; MYO1F, sc-376534; Santa Cruz; CD33, ab269456; Abcam). The nuclei were stained with DAPI before sealing, and all sections were scanned by the automated multispectral microscopy system Vectra 3.0 (PerkinElmer).

RT-qPCR

RNA was extracted using TRIzol Reagent (Invitrogen), and cDNA was synthesized by RT of total RNA (Applied Biosystems) following standard procedures. The primer sequences (5'-3') used are as follows: Myolf F: 5'-CTTTCACTGGCAGAGTCACAA-3', R: 5'-ATGAAGCGTTTGCGGAGGTT-3'; Illb F: 5'-GAAATGCCACCT TTTGACAGTG-3', 5'-TGGATGCTCTCATCAGGACAG-3'; Nos2 F: 5'-GTTCTCAGCCCAACAATACAAGA-3', R: 5'-GTGGACGGGTCG ATGTCAC-3'; Ccl5 F: 5'-GCTGCTTTGCCTACCTCTCC-3', R: 5'-TCGAGTGACAAACACGACTGC-3'; Cd274 F: 5'-GCTCCAAAGGAC TTGTACGTG-3', R: 5'-TGATCTGAAGGGCAGCATTTC-3'; Il10 F: 5'-GCTCTTACTGACTGGCATGAG-3', R: 5'-CGCAGCTCTAGG AGCATGTG-3'; Cybb F: 5'-TGTGGTTGGGGCTGAATGTC-3', R: 5'-CTGAGAAAGGAGAGCAGATTTCG-3'; Arg1 F: 5'-CTCCAAGCC AAAGTCCTTAGAG-3', R: 5'-AGGAGCTGTCATTAGGGACATC-3'; Ido1 F: 5'-GCTTTGCTCTACCACATCCAC-3', R: 5'-CAGGCG CTGTAACCTGTGT-3'; Ccl2 F: 5'-TTAAAAACCTGGATCGGAACC AA-3', R: 5'-GCATTAGCTTCAGATTTACGGGT-3'; Nox1 F: 5'-GGT TGGGGCTGAACATTTTTC-3', R: 5'-TCGACACACAGGAATCAG GAT-3'; Nox3 F: 5'-CAACGCACAGGCTCAAATGG-3', R: 5'-CAC TCTCGTTCAGAATCCAGC-3'; Nox4 F: 5'-GAAGGGGTTAAACAC CTCTGC-3', R: 5'-ATGCTCTGCTTAAACACAATCCT-3'; Duox1 F: 5'-AAAACACCAGGAACGGATTGT-3', R: 5'-AGAAGACATTGG GCTGTAGGG-3'; and Duox2 F: 5'-AAGTTCAAGCAGTACAAGCGA T-3', R: 5'-TAGGCACGGTCTGCAAACAG-3'.

Relative gene expression was determined using the $\Delta\Delta^{-ct}$ method versus the housekeeping gene *Gapdh*.



In vitro chemotaxis assay

For neutrophil migration under CXCL2 treatment. Cultured neutrophil of day 4 were starved for 24 h with serum-free medium and dissociated by Trypsin-EDTA (0.05%) (25300054; Gibco). Suspended cells were washed and resuspend in serumfree RPMI 1640 medium at 3×10^6 cells/ml. 5- μ m pore transwell insert (Corning) was precoated inside the upper chamber with Matrigel (356231; Corning) and placed in 24-well plate. Medium containing CXCL2 (100 ng/ml) (25015; PeproTech) were added in the 24-well plate with 650 μl and suspended neutrophils were added into the upper chamber with 200 µl. After 6 h at 37°C and 5% CO₂, the insert was collected and fixed/stained with 4% formaldehyde solution and 0.5% crystal violet solution. After wiping the inner layer with a cotton swab, the number of cells that had migrated was quantitated by counting the mean number of cells in four randomly selected areas per well (magnification: ×200) under microscope. For CD8+ T chemotaxis, CD8+ T was sorted with CD8+ T Cell Isolation Kit (Cat #19853; STEMCELL) and resuspend in serum-free RPMI 1640 medium at 2×10^7 cells/ml, and 200 μ l suspension was added into the precoated upper chamber of 5-µm pore transwell. Neutrophils (3×10^6 cells/well) or cell lysate were placed into the 24-well plate with 650 μ l. Cell lysate was obtained from 2 \times 107 cells/ml by ultrasonication under 4°C in cold PBS and centrifuged at 10,000 rpm containing protease inhibitors (P8340; Sigma-Aldrich). After 6 h, CD8+ T cell in the lower chamber counts by FACS with anti-CD8 flow staining with different treatment.

Co-IP

Cells were lysed in non-denaturing NP-40 lysis buffer (50 mM Tris HCl, pH 7.4, 0.25% sodium deoxycholate, 150 mM NaCl, 1 mM EDTA, and 1% NP-40) supplemented with 1 mM PMSF, 1 mM dithiothreitol (DTT), 1× PhosStop, and 1× protease inhibitor Complete Mini EDTA-free. For each reaction, 1 mg of total protein was immunoprecipitated using 50 μ l Dynabeads Protein G (Thermo Fisher Scientific) incubated with 2 μ g of primary antibody in PBST while agitating overnight at 4°C. After several washing steps, the precipitated protein fraction was eluted by shaking the beads in 20 μ l of 1× loading buffer (62.5 mM Tris, pH 6.8, 2% SDS, 10% glycerol, 25 mM DTT, and 0.01% bromophenol blue) for 15 min at room temperature. The supernatant containing the IP fraction was boiled for 5 min at 95°C before SDS-PAGE and western blot analysis.

In vitro co-culture of neutrophils and CD8+ T cells

Neutrophils were isolated by flow sorting from tumor tissues of WT and *Myolf*^{-/-} mice as described above. CD8⁺ T cell were isolated from the spleens of naïve C57BL/6 WT mice using a Mouse CD8⁺ T Cell Isolation kit (Cat #19853; STEMCELL) according to the manufacturer's instructions. Splenic CD8⁺ T cells were stained with 2 nM CFSE for 5 min at 37°C. The CFSE-labeled T cells were co-cultured with neutrophils (1:4 ratio) in RPMI-1640 medium with GlutaMAX (supplemented as for neutrophil vitality) for 72 h in 96-well round bottom plates precoated for 3 h with anti-CD3 (100 ng/ml, clone 37.51) and anti-CD28 antibodies (50 ng/ml, clone 17A2; both eBioscience).

The proliferation of CD8⁺ T cell was assessed after 72 h of co-culture by measuring CFSE dilution using the BD FACS LSRFortessa flow cytometer.

siRNA and shRNA transfection

For siRNA transfection, cultured neutrophils (2×10^5 cells) were transfected with scrambled or target siRNA duplexes (2 nM) using siRNA Transfection Medium (jetPRIME, polyplus) according to the manufacturer's instructions. After 24 h, the medium was replaced with RPMI 10% FBS (500 μ l), and the cells were incubated for an additional 24 h. Efficacy of the target silencing was determined by western blotting in the cell lysates or by q-PCR. siRNA-Myolf used here was described in our previous publication (Wang et al., 2021b). siRNA-Cd274 (SC-39700) and siRNA-Cxcl9 (SC-60027) were from Santa Cruz. siRNA-Phb1 sequence of 5'-AGGAUAAGCCCAAAUGUU GCC-3'.

For gene silencing using shRNA lentivirus, targeting guide of 5′-GCCGTAAGATGGACAGCAAAT-3′ was cloned into shRNA lentiviral plasmid of PLKO.1-puro vector. Functional sequences in the shRNA vectors are as follows: 5′-CCGGGCCGTAAGATG GACAGCAAATCTCGAGATTTGCTGTCCATCTTACGGCTTTTTG-3′. For the generation of lentiviral particles, 293FT cells were co-transfected with the plasmid pLKO.1-puro and lentiviral packaging mix using Lipo3000 (PLKO.1:psPAX2:pMD2.G = 3:1:1) (L3000015; Invitrogen), and supernatants containing lentivirus were harvested and concentrated (C2901S, Virus Concentration Kit; Beyotime) at 48 h after transfection. For lentiviral transduction, MC38 and B16F10 cells were treated with concentrated virus from 293FT cells in the presence of 10 μ g/ml polybrene, and stable cell lines expressing shRNA were generated by selection with puromycin (8 μ g/ml).

Construction of sgRNA-expressed B16F10 cell line

The lentiCRISPR v2 (No. 52961; Addgene) was digested by Esp3i and recovered through agar gel electrophoresis. The annealed sgRNA (5'-AGCACTAGAAGCCACGGGAG-3') was ligated to the recovered digested product by a rapid ligase. The ligation product was transferred to DH5α competent cells (Sangon), and the clones were screened on ampicillin-resistant LB plates. The positive clones were screened and sequenced by Sangon Biotech. The recombinant plasmid was extracted from the correct clones. The constructed lentiCRISPR v2-sgRNA plasmid and two other lentiviral packaging plasmids psPAX2 (no. 12260; Addgene) and pMD2.G (no. 12259; Addgene) were co-transfected into HEK293FT cells at a molar ratio of 2:1:1 using the Lipofectamine 3000 Transfection Reagent Kit (Invitrogen). At 60 h after transfection, the lentivirus was harvested and centrifuged in 1.5ml eppendorf tube at 15,000 \times q at 4°C for 5 min. The supernatant was retained and filtered with a 0.45-µm filter before using. B16F10 cells were seeded into 24-well plate and infected with 200 µl of the packaged lentivirus. The next day, 5 µg/ml puromycin was added to the cell supernatant for drug screening. Cells were diluted and seeded into 96-well plates with one cell per well at day 4. After the single cell grew into a cell mass, the monoclonal cell mass was digested and moved to a 6-well plate to continue the culture.



BSP methylation sequencing

Cultured neutrophils in vitro (day 5) were starved for 36 h before treating with TGF-β1 or for another 24 h. Neutrophils were collected, and genomic DNA was extracted using a QIAamp DNA kit (Cat #51306; Qiagen). Genomic DNA was modified and purified using an EpiTect Fast DNA bisulfite kit (Cat #59824; Qiagen). 300 ng of converted DNA was stored at -20°C until required for use. A 50 ng quantity of converted DNA was used in a 50 µl reaction system with BSP primers. These PCR products were cloned into a pMD19-T vector. 10 clones per sample were sequenced. The methylation levels were evaluated by calculating the percentage of converted cytosines to the total number of cytosines. Primers were designed using Methyl Primer Express v1.0 software to amplify CG island fragments in the target region. For the target sequence region to be detected, use the CpG island analysis software CpGPlot provided by the European EBI website for online analysis of genomic DNA sequences (https://www.ebi.ac.uk/Tools/seqstats/emboss_ cpgplot/). TA cloning sequencing results were analyzed using BiQ Analyzer software.

Primers used are as follows: Myo1f-1-NF: 5'-TAGATATTT ATAAGGTGGAAGGTAT-3'; Myo1f-1-NR: 5'-CCTATCTCTACTAC CCCAATACTA-3'; Myo1f-1-WF: 5'-TTTAGGAGTAGTAGTAGAA TTTAGGAT-3'; and Myo1f-1-WR: 5'-ATTAACTAATTTAATCAA ACCAAATA-3'.

Online supplemental material

Fig. S1 shows the correlation of MYO1F level and ICB response. Fig. S2 shows the regulation of MYO1F deficiency on tumor growth and the gating strategy of distribution and sorting of neutrophils. Fig. S3 contains the analysis of neutrophil in circulation and supporting data from conditional KO mice (Myo1 $f^{E/f}$ -S100A8cre). Fig. S4 contains the ROS production and the combination of neutrophil to CD8+ T cell. Fig. S5 contains the provenance of TGF-β1 and the prediction of binding sites of SPI in MYO1F.

Data availability

RNA-Seq data in this study have been deposited in the Sequence Read Archive (accession PRJNA1224833). The reanalyzed data in Fig. 1 A and Fig. S1, A and B are openly available in the National Library of Medicine under accession nos. PRJEB23709 (ALL), PRJEB23709 (α -PD-1), PRJEB23709 (α -PD-1 + α -CTLA-4), and PRJNA306069 (Melanoma-Nathanson_2017_α-CTLA-4). The reanalyzed data in Fig. 1 B and Fig. S1 F are openly available in The Cancer Genome Atlas with Ensembl ID: ENSG00000142347. The reanalyzed data of Fig. 1, D and E are openly available in the National Library of Medicine Sequence Read Archive under accession nos. SRP183455 (PRJNA520852), SRP217040 (PRJNA557841), ERP105482 (PRJEB23709), SRP150548 (PRJNA476140), SRP128156 (PRJNA420786), SRP011540 (PRJNA82747), SRP070710 (PRJNA312948), SRP094781 (PRJNA356761), SRP230414 (PRJN A578193), SRP250849 (PRJNA608935), and SRP302761 (PRJNA 693857). The reanalyzed SPI1-CHIP-seq results are openly available in the National Library of Medicine Gene Expression Omnibus under accession nos. GSM1875484, GSM2863951, GSM1531741, GSM1167581, GSM2634690, and GSM1133498.

Acknowledgments

We would like to thank Prof. Lai Guan Ng and Prof. Jing Wang for helpful discussion.

This study was supported by grants from the National Key Research and Development Program of China (2022YFA 0912400), the National Natural Science Foundation of China (82230055), the Technology Committee of Shanghai Municipality (23DX1900302), Shanghai Shu Guang Scholar, the Innovative Research Team of High-level Local Universities in Shanghai, the Shanghai Jiao Tong University Global Strategic Partnership Fund, and the grant from the State Key Laboratory of Medical Genomics.

Author contributions: Y. Qu: Conceptualization, data curation, formal analysis, investigation, methodology, project administration, validation, visualization, and writing—original draft, review, and editing. W. Liang: data curation, formal analysis, investigation, and writing—original draft, review, and editing. M. Yu: resources. C. Wang: resources. M. Luo: writing—review and editing. L. Zhong: supervision. Z. Li: funding acquisition, project administration, resources, and supervision. F. Wang: conceptualization, funding acquisition, investigation, project administration, resources, supervision, and writing—original draft, review, and editing.

Disclosures: The authors declare no competing interests exist.

Submitted: 22 October 2024 Revised: 29 January 2025 Accepted: 21 February 2025

References

Alomari, M. 2021. TRIM21 - a potential novel therapeutic target in cancer. Pharmacol. Res. 165:105443. https://doi.org/10.1016/j.phrs.2021.105443

Antuamwine, B.B., R. Bosnjakovic, F. Hofmann-Vega, X. Wang, T. Theodosiou, I. Iliopoulos, and S. Brandau. 2023. N1 versus N2 and PMN-MDSC: A critical appraisal of current concepts on tumor-associated neutrophils and new directions for human oncology. *Immunol. Rev.* 314:250–279. https://doi.org/10.1111/imr.13176

Araźna, M., M.P. Pruchniak, and U. Demkow. 2015. Reactive oxygen species, granulocytes, and NETosis. Adv. Exp. Med. Biol. 836:1-7. https://doi.org/ 10.1007/5584 2014 12

Bitsch, R., A. Kurzay, F. Özbay Kurt, C. De La Torre, S. Lasser, A. Lepper, A. Siebenmorgen, V. Müller, P. Altevogt, J. Utikal, and V. Umansky. 2022. STAT3 inhibitor Napabucasin abrogates MDSC immunosuppressive capacity and prolongs survival of melanoma-bearing mice. J. Immunother. Cancer. 10:e004384. https://doi.org/10.1136/jitc-2021-004384

Bornstein, C., D. Winter, Z. Barnett-Itzhaki, E. David, S. Kadri, M. Garber, and I. Amit. 2014. A negative feedback loop of transcription factors specifies alternative dendritic cell chromatin States. Mol. Cell. 56:749–762. https://doi.org/10.1016/j.molcel.2014.10.014

Bronte, V., P. Serafini, E. Apolloni, and P. Zanovello. 2001. Tumor-induced immune dysfunctions caused by myeloid suppressor cells. *J. Immunother*. 24:431–446. https://doi.org/10.1097/00002371-200111000-00001

Browne, E.P. 2015. An interleukin-1 beta-encoding retrovirus exhibits enhanced replication in vivo. *J. Virol.* 89:155–164. https://doi.org/10.1128/JVI.02314-14

Budimir, N., G.D. Thomas, J.S. Dolina, and S. Salek-Ardakani. 2022. Reversing T-cell exhaustion in cancer: Lessons learned from PD-1/PD-L1 immune checkpoint blockade. Cancer Immunol. Res. 10:146–153. https://doi.org/ 10.1158/2326-6066.CIR-21-0515

Calero-Nieto, F.J., F.S. Ng, N.K. Wilson, R. Hannah, V. Moignard, A.I. Leal-Cervantes, I. Jimenez-Madrid, E. Diamanti, L. Wernisch, and B. Göttgens. 2014. Key regulators control distinct transcriptional programmes in



- blood progenitor and mast cells. EMBO J. 33:1212–1226. https://doi.org/10.1002/embj.201386825
- Calon, A., E. Espinet, S. Palomo-Ponce, D.V. Tauriello, M. Iglesias, M.V. Céspedes, M. Sevillano, C. Nadal, P. Jung, X.H. Zhang, et al. 2012. Dependency of colorectal cancer on a TGF- β -driven program in stromal cells for metastasis initiation. *Cancer Cell*. 22:571–584. https://doi.org/10.1016/j.ccr.2012.08.013
- Carey, H.A., B.E. Hildreth III, J.A. Geisler, M.C. Nickel, J. Cabrera, S. Ghosh, Y. Jiang, J. Yan, J. Lee, S. Makam, et al. 2018. Enhancer variants reveal a conserved transcription factor network governed by PU.1 during osteoclast differentiation. *Bone Res.* 6:8. https://doi.org/10.1038/s41413-018-0011-1
- Castro-Mondragon, J.A., R. Riudavets-Puig, I. Rauluseviciute, R.B. Lemma, L. Turchi, R. Blanc-Mathieu, J. Lucas, P. Boddie, A. Khan, N. Manosalva Pérez, et al. 2022. JASPAR 2022: The 9th release of the open-access database of transcription factor binding profiles. *Nucleic Acids Res.* 50: D165–D173. https://doi.org/10.1093/nar/gkab1113
- Chen, L.C., C. Hsu, C.C. Chiueh, and W.S. Lee. 2012. Ferrous citrate upregulates the NOS2 through nuclear translocation of NFkB induced by free radicals generation in mouse cerebral endothelial cells. *PLoS One.* 7: e46239. https://doi.org/10.1371/journal.pone.0046239
- Chen, Z., Z. Luo, D. Zhang, H. Li, X. Liu, K. Zhu, H. Zhang, Z. Wang, P. Zhou, J. Ren, et al. 2023. TIGER: A web portal of tumor immunotherapy gene expression Resource. *Genomics Proteomics Bioinformatics*. 21:337–348. https://doi.org/10.1016/j.gpb.2022.08.004
- Chin, A.L., S. Jiang, E. Jang, L. Niu, L. Li, X. Jia, and R. Tong. 2021. Implantable optical fibers for immunotherapeutics delivery and tumor impedance measurement. *Nat. Commun.* 12:5138. https://doi.org/10.1038/s41467-021-25391-z
- Chow, M.T., A.J. Ozga, R.L. Servis, D.T. Frederick, J.A. Lo, D.E. Fisher, G.J. Freeman, G.M. Boland, and A.D. Luster. 2019. Intratumoral activity of the CXCR3 chemokine system is required for the efficacy of anti-PD-1 therapy. *Immunity*. 50:1498–1512.e5. https://doi.org/10.1016/j.immuni.2019.04.010
- Chung, A.W., K. Anand, A.C. Anselme, A.A. Chan, N. Gupta, L.A. Venta, M.R. Schwartz, W. Qian, Y. Xu, L. Zhang, et al. 2021. A phase 1/2 clinical trial of the nitric oxide synthase inhibitor L-NMMA and taxane for treating chemoresistant triple-negative breast cancer. *Sci. Transl. Med.* 13: eabj5070. https://doi.org/10.1126/scitranslmed.abj5070
- Condamine, T., and D.I. Gabrilovich. 2011. Molecular mechanisms regulating myeloid-derived suppressor cell differentiation and function. *Trends Immunol.* 32:19–25. https://doi.org/10.1016/j.it.2010.10.002
- Correale, J. 2021. Immunosuppressive amino-acid catabolizing enzymes in multiple sclerosis. Front. Immunol. 11:600428. https://doi.org/10.3389/fimmu.2020.600428
- Davis, R.J., E.C. Moore, P.E. Clavijo, J. Friedman, H. Cash, Z. Chen, C. Silvin, C. Van Waes, and C. Allen. 2017. Anti-PD-L1 efficacy can Be enhanced by inhibition of myeloid-derived suppressor cells with a selective inhibitor of PI3Kδ/γ. *Cancer Res.* 77:2607–2619. https://doi.org/10.1158/0008-5472.CAN-16-2534
- de Coaña, Y.P., M. Wolodarski, I. Poschke, Y. Yoshimoto, Y. Yang, M. Nyström, U. Edbäck, S.E. Brage, A. Lundqvist, G.V. Masucci, et al. 2017. Ipilimumab treatment decreases monocytic MDSCs and increases CD8 effector memory T cells in long-term survivors with advanced melanoma. Oncotarget. 8:21539-21553. https://doi.org/10.18632/oncotarget.15368
- Deng, H., A. Kan, N. Lyu, M. He, X. Huang, S. Qiao, S. Li, W. Lu, Q. Xie, H. Chen, et al. 2021. Tumor-derived lactate inhibit the efficacy of lenvatinib through regulating PD-L1 expression on neutrophil in hepatocellular carcinoma. J. Immunother. Cancer. 9:e002305. https://doi.org/10.1136/jitc-2020-002305
- Diquigiovanni, C., C. Bergamini, C. Evangelisti, F. Isidori, A. Vettori, N. Tiso, F. Argenton, A. Costanzini, L. Iommarini, H. Anbunathan, et al. 2018. Mutant MYO1F alters the mitochondrial network and induces tumor proliferation in thyroid cancer. *Int. J. Cancer*. 143:1706–1719. https://doi.org/10.1002/ijc.31548
- Dolina, J.S., N. Van Braeckel-Budimir, G.D. Thomas, and S. Salek-Ardakani. 2021. CD8+ T cell exhaustion in cancer. Front. Immunol. 12:715234. https://doi.org/10.3389/fimmu.2021.715234
- Duhoux, F.P., G. Ameye, J.M. Libouton, K. Bahloula, S. Iossifidis, C.F. Chantrain, J.B. Demoulin, and H.A. Poirel. 2011. The t(11;19)(q23;p13) fusing MLL with MYO1F is recurrent in infant acute myeloid leukemias. *Leuk. Res.* 35:e171–e172. https://doi.org/10.1016/j.leukres.2011.04.022
- Eckert, I., E. Ribechini, and M.B. Lutz. 2021. In vitro generation of murine myeloid-derived suppressor cells, analysis of markers, developmental

- commitment, and function. *Methods Mol. Biol.* 2236:99–114. https://doi.org/10.1007/978-1-0716-1060-2_10
- Eichenfield, D.Z., T.D. Troutman, V.M. Link, M.T. Lam, H. Cho, D. Gosselin, N.J. Spann, H.P. Lesch, J. Tao, J. Muto, et al. 2016. Tissue damage drives co-localization of NF-μB, Smad3, and Nrf2 to direct Rev-erb sensitive wound repair in mouse macrophages. *Elife*. 5:el3024. https://doi.org/10.7554/eLife.13024
- Evrard, M., I.W.H. Kwok, S.Z. Chong, K.W.W. Teng, E. Becht, J. Chen, J.L. Sieow, H.L. Penny, G.C. Ching, S. Devi, et al. 2018. Developmental analysis of bone marrow neutrophils reveals populations specialized in expansion, trafficking, and effector functions. *Immunity*. 48:364–379.e8. https://doi.org/10.1016/j.immuni.2018.02.002
- Fossati, G., D.A. Moulding, D.G. Spiller, R.J. Moots, M.R. White, and S.W. Edwards. 2003. The mitochondrial network of human neutrophils: Role in chemotaxis, phagocytosis, respiratory burst activation, and commitment to apoptosis. *J. Immunol.* 170:1964–1972. https://doi.org/10.4049/jimmunol.170.4.1964
- Francis, D.M., M.P. Manspeaker, A. Schudel, L.F. Sestito, M.J. O'Melia, H.T. Kissick, B.P. Pollack, E.K. Waller, and S.N. Thomas. 2020. Blockade of immune checkpoints in lymph nodes through locoregional delivery augments cancer immunotherapy. Sci. Transl. Med. 12:eaay3575. https://doi.org/10.1126/scitranslmed.aay3575
- Fridlender, Z.G., J. Sun, S. Kim, V. Kapoor, G. Cheng, L. Ling, G.S. Worthen, and S.M. Albelda. 2009. Polarization of tumor-associated neutrophil phenotype by TGF-beta: "N1" versus "N2" TAN. Cancer Cell. 16:183–194. https://doi.org/10.1016/j.ccr.2009.06.017
- Gabrilovich, D.I., and S. Nagaraj. 2009. Myeloid-derived suppressor cells as regulators of the immune system. Nat. Rev. Immunol. 9:162–174. https://doi.org/10.1038/nri2506
- Gu, S.S., W. Zhang, X. Wang, P. Jiang, N. Traugh, Z. Li, C. Meyer, B. Stewig, Y. Xie, X. Bu, et al. 2021. Therapeutically increasing MHC-I expression potentiates immune checkpoint blockade. *Cancer Discov.* 11:1524–1541. https://doi.org/10.1158/2159-8290.CD-20-0812
- Guo, Y.C., Y.H. Chiu, C.P. Chen, and H.S. Wang. 2018. Interleukin-1β induces CXCR3-mediated chemotaxis to promote umbilical cord mesenchymal stem cell transendothelial migration. Stem Cell Res. Ther. 9:281. https://doi.org/10.1186/s13287-018-1032-9
- Hegde, S., A.M. Leader, and M. Merad. 2021. MDSC: Markers, development, states, and unaddressed complexity. *Immunity*. 54:875–884. https://doi.org/10.1016/j.immuni.2021.04.004
- Heinz, L.X., B. Platzer, P.M. Reisner, A. Jörgl, S. Taschner, F. Göbel, and H. Strobl. 2006. Differential involvement of PU.1 and Id2 downstream of TGF-betal during Langerhans-cell commitment. Blood. 107:1445–1453. https://doi.org/10.1182/blood-2005-04-1721
- Holokai, L., J. Chakrabarti, J. Lundy, D. Croagh, P. Adhikary, S.S. Richards, C. Woodson, N. Steele, R. Kuester, A. Scott, et al. 2020. Murine- and human-derived autologous organoid/immune cell Co-cultures as preclinical models of pancreatic ductal adenocarcinoma. Cancers (Basel). 12: 3816. https://doi.org/10.3390/cancers12123816
- Humblin, E., M. Thibaudin, F. Chalmin, V. Derangère, E. Limagne, C. Richard, R.A. Flavell, S. Chevrier, S. Ladoire, H. Berger, et al. 2017. IRF8dependent molecular complexes control the Th9 transcriptional program. Nat. Commun. 8:2085. https://doi.org/10.1038/s41467-017-01070 -W
- Im, S.J., M. Hashimoto, M.Y. Gerner, J. Lee, H.T. Kissick, M.C. Burger, Q. Shan, J.S. Hale, J. Lee, T.H. Nasti, et al. 2016. Defining CD8+ T cells that provide the proliferative burst after PD-1 therapy. *Nature*. 537:417-421. https://doi.org/10.1038/nature19330
- Jaillon, S., A. Ponzetta, D. Di Mitri, A. Santoni, R. Bonecchi, and A. Mantovani. 2020. Neutrophil diversity and plasticity in tumour progression and therapy. Nat. Rev. Cancer. 20:485-503. https://doi.org/10.1038/s41568 -020-0281-y
- Jiang, H., C. Gebhardt, L. Umansky, P. Beckhove, T.J. Schulze, J. Utikal, and V. Umansky. 2015. Elevated chronic inflammatory factors and myeloid-derived suppressor cells indicate poor prognosis in advanced melanoma patients. Int. J. Cancer. 136:2352–2360. https://doi.org/10.1002/ijc.29297
- Jordan, K.R., R.N. Amaria, O. Ramirez, E.B. Callihan, D. Gao, M. Borakove, E. Manthey, V.F. Borges, and M.D. McCarter. 2013. Myeloid-derived suppressor cells are associated with disease progression and decreased overall survival in advanced-stage melanoma patients. Cancer Immunol. Immunother. 62:1711–1722. https://doi.org/10.1007/s00262-013-1475-x
- Ju, J.M., G. Nam, Y.K. Lee, M. Jung, H. Chang, W. Kim, W.J. Shon, J.Y. Lim, J.Y. Kim, J. Chang, et al. 2021. IDO1 scavenges reactive oxygen species in myeloid-derived suppressor cells to prevent graft-versus-host disease.



- Proc. Natl. Acad. Sci. USA. 118:e2011170118. https://doi.org/10.1073/pnas.2011170118
- Jurkin, J., Y.M. Schichl, R. Koeffel, T. Bauer, S. Richter, S. Konradi, B. Gesslbauer, and H. Strobl. 2010. miR-146a is differentially expressed by myeloid dendritic cell subsets and desensitizes cells to TLR2-dependent activation. J. Immunol. 184:4955-4965. https://doi.org/10.4049/jimmunol.0903021
- Kang, K., X. Lin, P. Chen, H. Liu, F. Liu, W. Xiong, G. Li, M. Yi, X. Li, H. Wang, and B. Xiang. 2024. T cell exhaustion in human cancers. Biochim. Biophys. Acta Rev. Cancer. 1879:189162. https://doi.org/10.1016/j.bbcan.2024.189162
- Kathiria, A.S., W.L. Neumann, J. Rhees, E. Hotchkiss, Y. Cheng, R.M. Genta, S.J. Meltzer, R.F. Souza, and A.L. Theiss. 2012. Prohibitin attenuates colitis-associated tumorigenesis in mice by modulating p53 and STAT3 apoptotic responses. *Cancer Res.* 72:5778–5789. https://doi.org/10.1158/ 0008-5472.CAN-12-0603
- Kelly, E.K., L. Wang, and L.B. Ivashkiv. 2010. Calcium-activated pathways and oxidative burst mediate zymosan-induced signaling and IL-10 production in human macrophages. J. Immunol. 184:5545–5552. https://doi .org/10.4049/jimmunol.0901293
- Khoyratty, T.E., Z. Ai, I. Ballesteros, H.L. Eames, S. Mathie, S. Martín-Salamanca, L. Wang, A. Hemmings, N. Willemsen, V. von Werz, et al. 2021. Distinct transcription factor networks control neutrophil-driven inflammation. *Nat. Immunol.* 22:1093–1106. https://doi.org/10.1038/s41590-021-00968-4
- Kim, S.V., W.Z. Mehal, X. Dong, V. Heinrich, M. Pypaert, I. Mellman, M. Dembo, M.S. Mooseker, D. Wu, and R.A. Flavell. 2006. Modulation of cell adhesion and motility in the immune system by Myo1f. Science. 314: 136–139. https://doi.org/10.1126/science.1131920
- Kortylewski, M., M. Kujawski, T. Wang, S. Wei, S. Zhang, S. Pilon-Thomas, G. Niu, H. Kay, J. Mulé, W.G. Kerr, et al. 2005. Inhibiting Stat3 signaling in the hematopoietic system elicits multicomponent antitumor immunity. Nat. Med. 11:1314–1321. https://doi.org/10.1038/nm1325
- Kusmartsev, S., Y. Nefedova, D. Yoder, and D.I. Gabrilovich. 2004. Antigen-specific inhibition of CD8+ T cell response by immature myeloid cells in cancer is mediated by reactive oxygen species. J. Immunol. 172:989–999. https://doi.org/10.4049/jimmunol.172.2.989
- Lang, S., K. Bruderek, C. Kaspar, B. Höing, O. Kanaan, N. Dominas, T. Hussain, F. Droege, C. Eyth, B. Hadaschik, and S. Brandau. 2018. Clinical relevance and suppressive capacity of human myeloid-derived suppressor cell subsets. Clin. Cancer Res. 24:4834–4844. https://doi.org/10.1158/1078-0432.CCR-17-3726
- Lin, H., L. Feng, K.S. Cui, L.W. Zeng, D. Gao, L.X. Zhang, W.H. Xu, Y.H. Sun, H.B. Shu, and S. Li. 2021. The membrane-associated E3 ubiquitin ligase MARCH3 downregulates the IL-6 receptor and suppresses colitisassociated carcinogenesis. Cell. Mol. Immunol. 18:2648–2659. https:// doi.org/10.1038/s41423-021-00799-1
- Lyck, R., and G. Enzmann. 2015. The physiological roles of ICAM-1 and ICAM-2 in neutrophil migration into tissues. *Curr. Opin. Hematol.* 22:53–59. https://doi.org/10.1097/MOH.00000000000000103
- Martens, A., K. Wistuba-Hamprecht, M. Geukes Foppen, J. Yuan, M.A. Postow, P. Wong, E. Romano, A. Khammari, B. Dreno, M. Capone, et al. 2016. Baseline peripheral blood biomarkers associated with clinical outcome of advanced melanoma patients treated with ipilimumab. Clin. Cancer Res. 22:2908–2918. https://doi.org/10.1158/1078-0432.CCR-15-2412
- Matsumura, N., Z. Huang, S. Mori, T. Baba, S. Fujii, I. Konishi, E.S. Iversen, A. Berchuck, and S.K. Murphy. 2011. Epigenetic suppression of the TGF-beta pathway revealed by transcriptome profiling in ovarian cancer. *Genome Res.* 21:74–82. https://doi.org/10.1101/gr.108803.110
- McConnell, R.E., and M.J. Tyska. 2010. Leveraging the membrane cytoskeleton interface with myosin-1. *Trends Cell Biol.* 20:418–426. https://doi.org/10.1016/j.tcb.2010.04.004
- McMurray, J.S. 2006. A new small-molecule Stat3 inhibitor. *Chem. Biol.* 13: 1123–1124. https://doi.org/10.1016/j.chembiol.2006.11.001
- Meyer, C., L. Cagnon, C.M. Costa-Nunes, P. Baumgaertner, N. Montandon, L. Leyvraz, O. Michielin, E. Romano, and D.E. Speiser. 2014. Frequencies of circulating MDSC correlate with clinical outcome of melanoma patients treated with ipilimumab. Cancer Immunol. Immunother. 63: 247–257. https://doi.org/10.1007/s00262-013-1508-5
- Miao, N., Z. Wang, Q. Wang, H. Xie, N. Yang, Y. Wang, J. Wang, H. Kang, W. Bai, Y. Wang, et al. 2023. Oxidized mitochondrial DNA induces gasdermin D oligomerization in systemic lupus erythematosus. *Nat. Commun.* 14:872. https://doi.org/10.1038/s41467-023-36522-z
- Morad, G., B.A. Helmink, P. Sharma, and J.A. Wargo. 2022. Hallmarks of response, resistance, and toxicity to immune checkpoint blockade. Cell. 185:576. https://doi.org/10.1016/j.cell.2022.01.008

- Navinés-Ferrer, A., E. Ainsua-Enrich, E. Serrano-Candelas, J. Sayós, and M. Martin. 2019. Myolf, an unconventional long-tailed myosin, is a new partner for the adaptor 3BP2 involved in mast cell migration. Front. Immunol. 10:1058. https://doi.org/10.3389/fimmu.2019.01058
- Navinés-Ferrer, A., and M. Martín. 2020. Long-tailed unconventional class I myosins in health and disease. Int. J. Mol. Sci. 21:2555. https://doi.org/10.3390/ijms21072555
- Nefedova, Y., S. Nagaraj, A. Rosenbauer, C. Muro-Cacho, S.M. Sebti, and D.I. Gabrilovich. 2005. Regulation of dendritic cell differentiation and antitumor immune response in cancer by pharmacologic-selective inhibition of the janus-activated kinase 2/signal transducers and activators of transcription 3 pathway. *Cancer Res.* 65:9525–9535. https://doi.org/10.1158/0008-5472.CAN-05-0529
- Ng, L.G., R. Ostuni, and A. Hidalgo. 2019. Heterogeneity of neutrophils. Nat. Rev. Immunol. 19:255–265. https://doi.org/10.1038/s41577-019-0141-8
- Ng, M.S.F., I. Kwok, L. Tan, C. Shi, D. Cerezo-Wallis, Y. Tan, K. Leong, G.F. Calvo, K. Yang, Y. Zhang, et al. 2024. Deterministic reprogramming of neutrophils within tumors. *Science*. 383:eadf6493. https://doi.org/10.1126/science.adf6493
- Nott, A., S.H. Meislin, and M.J. Moore. 2003. A quantitative analysis of intron effects on mammalian gene expression. RNA. 9:607-617. https://doi.org/10.1261/rna.5250403
- Ochiai, K., M. Maienschein-Cline, G. Simonetti, J. Chen, R. Rosenthal, R. Brink, A.S. Chong, U. Klein, A.R. Dinner, H. Singh, and R. Sciammas. 2013. Transcriptional regulation of germinal center B and plasma cell fates by dynamical control of IRF4. *Immunity*. 38:918–929. https://doi.org/10.1016/j.immuni.2013.04.009
- Olson, M.C., E.W. Scott, A.A. Hack, G.H. Su, D.G. Tenen, H. Singh, and M.C. Simon. 1995. PU. 1 is not essential for early myeloid gene expression but is required for terminal myeloid differentiation. *Immunity*. 3:703–714. https://doi.org/10.1016/1074-7613(95)90060-8
- Paley, M.A., D.C. Kroy, P.M. Odorizzi, J.B. Johnnidis, D.V. Dolfi, B.E. Barnett, E.K. Bikoff, E.J. Robertson, G.M. Lauer, S.L. Reiner, and E.J. Wherry. 2012. Progenitor and terminal subsets of CD8+ T cells cooperate to contain chronic viral infection. *Science*. 338:1220–1225. https://doi.org/ 10.1126/science.1229620
- Pillay, J., I. den Braber, N. Vrisekoop, L.M. Kwast, R.J. de Boer, J.A. Borghans, K. Tesselaar, and L. Koenderman. 2010. In vivo labeling with 2H2O reveals a human neutrophil lifespan of 5.4 days. *Blood*. 116:625–627. https://doi.org/10.1182/blood-2010-01-259028
- Poschke, I., and R. Kiessling. 2012. On the armament and appearances of human myeloid-derived suppressor cells. *Clin. Immunol.* 144:250–268. https://doi.org/10.1016/j.clim.2012.06.003
- Prasad, S., S.C. Gupta, and A.K. Tyagi. 2017. Reactive oxygen species (ROS) and cancer: Role of antioxidative nutraceuticals. *Cancer Lett.* 387:95–105. https://doi.org/10.1016/j.canlet.2016.03.042
- Pruenster, M., T. Vogl, J. Roth, and M. Sperandio. 2016. S100A8/A9: From basic science to clinical application. *Pharmacol. Ther.* 167:120–131. https://doi.org/10.1016/j.pharmthera.2016.07.015
- Quail, D.F., B. Amulic, M. Aziz, B.J. Barnes, E. Eruslanov, Z.G. Fridlender, H.S. Goodridge, Z. Granot, A. Hidalgo, A. Huttenlocher, et al. 2022. Neutrophil phenotypes and functions in cancer: A consensus statement. J. Exp. Med. 219:e20220011. https://doi.org/10.1084/jem.20220011
- Qureshi, R., O. Yildirim, A. Gasser, C. Basmadjian, Q. Zhao, J.P. Wilmet, L. Désaubry, and C.G. Nebigil. 2015. FL3, a synthetic flavagline and ligand of prohibitins, protects cardiomyocytes via STAT3 from doxorubicin toxicity. PLoS One. 10:e0141826. https://doi.org/10.1371/journal.pone.0141826
- Ravindranathan, S., K.G. Nguyen, S.L. Kurtz, H.N. Frazier, S.G. Smith, B.P. Koppolu, N. Rajaram, and D.A. Zaharoff. 2018. Tumor-derived granulocyte colony-stimulating factor diminishes efficacy of breast tumor cell vaccines. *Breast Cancer Res.* 20:126. https://doi.org/10.1186/s13058-018-1054-3
- Sade-Feldman, M., J. Kanterman, Y. Klieger, E. Ish-Shalom, M. Olga, A. Saragovi, H. Shtainberg, M. Lotem, and M. Baniyash. 2016. Clinical significance of circulating CD33+CD11b+HLA-DR- myeloid cells in patients with stage IV melanoma treated with ipilimumab. Clin. Cancer Res. 22:5661-5672. https://doi.org/10.1158/1078-0432.CCR-15-3104
- Sarri, N., K. Wang, M. Tsioumpekou, C. Castillejo-López, J. Lennartsson, C.H. Heldin, and N. Papadopoulos. 2022. Deubiquitinating enzymes USP4 and USP17 finetune the trafficking of PDGFRβ and affect PDGF-BB-induced STAT3 signalling. Cell. Mol. Life Sci. 79:85. https://doi.org/10 .1007/s00018-022-04128-1
- Scapini, P., J.A. Lapinet-Vera, S. Gasperini, F. Calzetti, F. Bazzoni, and M.A. Cassatella. 2000. The neutrophil as a cellular source of chemokines.



- Immunol. Rev. 177:195-203. https://doi.org/10.1034/j.1600-065x.2000
- Schmielau, J., and O.J. Finn. 2001. Activated granulocytes and granulocytederived hydrogen peroxide are the underlying mechanism of suppression of t-cell function in advanced cancer patients. Cancer Res. 61: 4756–4760.
- Shojaei, F., M. Singh, J.D. Thompson, and N. Ferrara. 2008. Role of Bv8 in neutrophil-dependent angiogenesis in a transgenic model of cancer progression. Proc. Natl. Acad. Sci. USA. 105:2640-2645. https://doi.org/ 10.1073/pnas.0712185105
- Sun, W., X. Ma, H. Wang, Y. Du, J. Chen, H. Hu, R. Gao, R. He, Q. Peng, Z. Cui, et al. 2021. MYO1F regulates antifungal immunity by regulating acetylation of microtubules. Proc. Natl. Acad. Sci. USA. 118:e2100230118. https://doi.org/10.1073/pnas.2100230118
- Szuster-Ciesielska, A., E. Hryciuk-Umer, A. Stepulak, K. Kupisz, and M. Kandefer-Szerszeń. 2004. Reactive oxygen species production by blood neutrophils of patients with laryngeal carcinoma and antioxidative enzyme activity in their blood. Acta Oncol. 43:252–258. https://doi.org/10.1080/02841860410029708
- Taki, T., M. Akiyama, S. Saito, R. Ono, M. Taniwaki, Y. Kato, Y. Yuza, Y. Eto, and Y. Hayashi. 2005. The MYO1F, unconventional myosin type 1F, gene is fused to MLL in infant acute monocytic leukemia with a complex translocation involving chromosomes 7, 11, 19 and 22. Oncogene. 24: 5191–5197. https://doi.org/10.1038/sj.onc.1208711
- Tang, L.Y., M. Heller, Z. Meng, L.R. Yu, Y. Tang, M. Zhou, and Y.E. Zhang. 2017. Transforming growth factor-β (TGF-β) directly activates the JAK1-STAT3 Axis to induce hepatic fibrosis in coordination with the SMAD pathway. J. Biol. Chem. 292:4302–4312. https://doi.org/10.1074/jbc.M116 .773085
- Tang, Z., B. Kang, C. Li, T. Chen, and Z. Zhang. 2019. GEPIA2: An enhanced web server for large-scale expression profiling and interactive analysis. Nucleic Acids Res. 47:W556-W560. https://doi.org/10.1093/nar/gkz430
- Teixeira, M.M. 2018. Myolf is critical for neutrophil migration in vivo. Blood. 131:1879–1880. https://doi.org/10.1182/blood-2018-03-837872
- Vasquez-Dunddel, D., F. Pan, Q. Zeng, M. Gorbounov, E. Albesiano, J. Fu, R.L. Blosser, A.J. Tam, T. Bruno, H. Zhang, et al. 2013. STAT3 regulates arginase-I in myeloid-derived suppressor cells from cancer patients. J. Clin. Invest. 123:1580-1589. https://doi.org/10.1172/JCI60083
- Wang, C., X. Zheng, J. Zhang, X. Jiang, J. Wang, Y. Li, X. Li, G. Shen, J. Peng, P. Zheng, et al. 2023. CD300ld on neutrophils is required for tumour-driven immune suppression. *Nature*. 621:830–839. https://doi.org/10.1038/s41586-023-06511-9
- Wang, H., Z. Cui, W. Sun, M. Yi, Y. Cheng, Y. Zhang, Y. Du, T. Pan, R. Gao, L. Feng, et al. 2025. MYO1F positions cGAS on the plasma membrane to ensure full and functional signaling. *Mol. Cell*. 85:150–165.e7. https://doi.org/10.1016/j.molcel.2024.11.026
- Wang, H., Y. Zhou, L. Oyang, Y. Han, L. Xia, J. Lin, Y. Tang, M. Su, S. Tan, Y. Tian, et al. 2019. LPLUNC1 stabilises PHB1 by counteracting TRIM21-mediated ubiquitination to inhibit NF-kB activity in nasopharyngeal carcinoma. *Oncogene*. 38:5062–5075. https://doi.org/10.1038/s41388-019-0778-6
- Wang, J.F., Y.P. Wang, J. Xie, Z.Z. Zhao, S. Gupta, Y. Guo, S.H. Jia, J. Parodo, J.C. Marshall, and X.M. Deng. 2021a. Upregulated PD-L1 delays human neutrophil apoptosis and promotes lung injury in an experimental mouse model of sepsis. Blood. 138:806–810. https://doi.org/10.1182/blood.2020009417

- Wang, Q., J. Huang, H. Sun, J. Liu, J. Wang, Q. Wang, Q. Qin, S. Mei, C. Zhao, X. Yang, et al. 2014. CR Cistrome: A ChIP-seq database for chromatin regulators and histone modification linkages in human and mouse. Nucleic Acids Res. 42:D450-D458. https://doi.org/10.1093/nar/gkt1151
- Wang, Y., X. Zhao, M. Gao, X. Wan, Y. Guo, Y. Qu, Y. Chen, T. Li, H. Liu, M. Jiang, et al. 2021b. Myosin 1f-mediated activation of microglia contributes to the photoreceptor degeneration in a mouse model of retinal detachment. Cell Death Dis. 12:926. https://doi.org/10.1038/s41419-021-03983-3
- Weber, J., G. Gibney, R. Kudchadkar, B. Yu, P. Cheng, A.J. Martinez, J. Kroeger, A. Richards, L. McCormick, V. Moberg, et al. 2016. Phase I/II study of metastatic melanoma patients treated with nivolumab who had progressed after ipilimumab. Cancer Immunol. Res. 4:345–353. https://doi.org/10.1158/2326-6066.CIR-15-0193
- Weide, B., A. Martens, H. Zelba, C. Stutz, E. Derhovanessian, A.M. Di Giacomo, M. Maio, A. Sucker, B. Schilling, D. Schadendorf, et al. 2014. Myeloid-derived suppressor cells predict survival of patients with advanced melanoma: Comparison with regulatory T cells and NY-ESO-1-or melan-A-specific T cells. Clin. Cancer Res. 20:1601-1609. https://doi.org/10.1158/1078-0432.CCR-13-2508
- Wolf, Y., A.C. Anderson, and V.K. Kuchroo. 2020. TIM3 comes of age as an inhibitory receptor. Nat. Rev. Immunol. 20:173–185. https://doi.org/10 .1038/s41577-019-0224-6
- Xun, Z., H. Zhou, M. Shen, Y. Liu, C. Sun, Y. Du, Z. Jiang, L. Yang, Q. Zhang, C. Lin, et al. 2024. Identification of hypoxia-ALCAM^{high} macrophage- exhausted T cell Axis in tumor microenvironment remodeling for immunotherapy resistance. Adv. Sci. (Weinh.). 11:e2309885. https://doi.org/10.1002/advs.202309885
- Yang, M., Y.R. Miao, G.Y. Xie, M. Luo, H. Hu, H.F. Kwok, J. Feng, and A.Y. Guo. 2022. ICBatlas: A comprehensive resource for depicting immune checkpoint blockade therapy characteristics from transcriptome profiles. Cancer Immunol. Res. 10:1398–1406. https://doi.org/10.1158/2326-6066.CIR-22-0249
- Yin, H., S. Gao, Q. Chen, S. Liu, S. Shoucair, Y. Ji, W. Lou, J. Yu, W. Wu, and N. Pu. 2022. Tumor-associated N1 and N2 neutrophils predict prognosis in patients with resected pancreatic ductal adenocarcinoma: A preliminary study. *MedComm*. 3:e183. https://doi.org/10.1002/mco2.183
- Youn, J.I., S. Nagaraj, M. Collazo, and D.I. Gabrilovich. 2008. Subsets of myeloid-derived suppressor cells in tumor-bearing mice. J. Immunol. 181:5791–5802. https://doi.org/10.4049/jimmunol.181.8.5791
- Zhang, B., Z. Wang, L. Wu, M. Zhang, W. Li, J. Ding, J. Zhu, H. Wei, and K. Zhao. 2013. Circulating and tumor-infiltrating myeloid-derived suppressor cells in patients with colorectal carcinoma. PLoS One. 8:e57114. https://doi.org/10.1371/journal.pone.0057114
- Zhang, J., J. Gu, X. Wang, C. Ji, D. Yu, M. Wang, J. Pan, H.A. Santos, H. Zhang, and X. Zhang. 2024. Engineering and targeting neutrophils for cancer therapy. Adv. Mater. 36:e2310318. https://doi.org/10.1002/adma.202310318
- Zhang, Q., L. Chen, B.T. Helfand, T.L. Jang, V. Sharma, J. Kozlowski, T.M. Kuzel, L.J. Zhu, X.J. Yang, B. Javonovic, et al. 2011. TGF-β regulates DNA methyltransferase expression in prostate cancer, correlates with aggressive capabilities, and predicts disease recurrence. PLoS One. 6: e25168. https://doi.org/10.1371/journal.pone.0025168
- Zhou, S., T. Su, F. Cheng, J. Cole, X. Liu, B. Zhang, S. Alam, J. Liu, and G. Zhu. 2024. Engineering cGAS-agonistic oligonucleotides as therapeutics for cancer immunotherapy. Mol. Ther. Nucleic Acids. 35:102126. https://doi.org/10.1016/j.omtn.2024.102126



Supplemental material



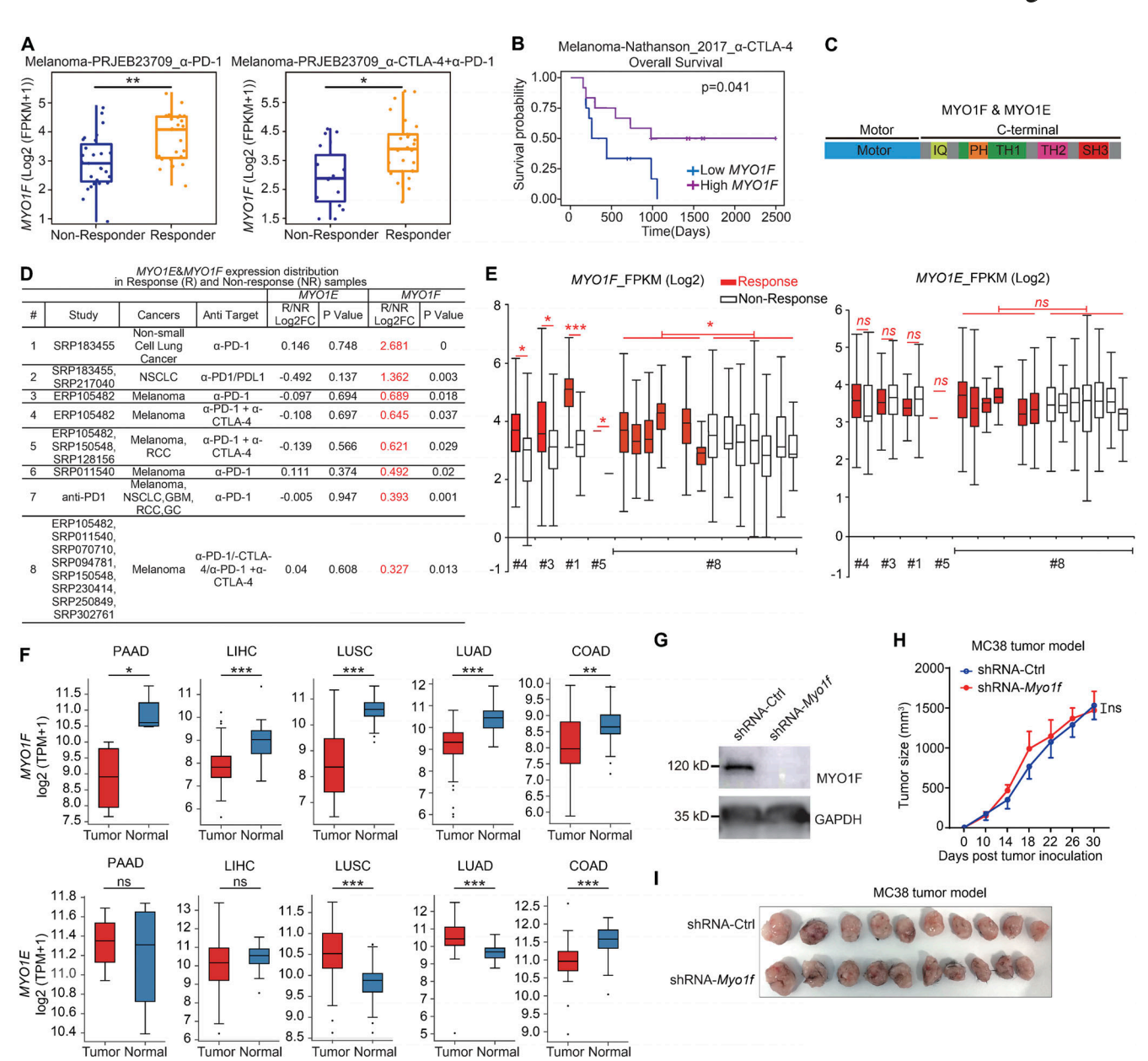


Figure S1. **Low level of MYO1F** in clinical tumors is associated with low ICB response. (A) Left: MYO1F gene expression pooled from responder (N = 23) and nonresponder (N = 27) of PRJEB23709_anti-PD-1 datasets. Right: MYO1F gene expression pooled from responder (N = 32) and nonresponder (N = 15) of PRJEB23709_anti-CTLA-4 datasets (TIGER database). P values were analyzed by Wilcoxon signed-rank test, *P < 0.05, **P < 0.01, ***P < 0.001. (B) Kaplan-Meier survival curves of Melanoma-Nathanson_2017_anti_CTLA-4 (TIGER database). P values were analyzed by log-rank test (Mantel-Cox), *P < 0.05, **P < 0.01, ***P < 0.001. (C) Schematic diagram of protein structure of MYO1F and MYO1E. (D) MYO1F and MYO1E gene expression in responder and nonresponder datasets from different immunotherapies datasets (ICBatlas database). (E) Statistic plots of MYO1F and MYO1E gene expression in responder and nonresponder datasets described in D (ICBatlas database). P values were analyzed by one-way ANOVA test, *P < 0.05, **P < 0.01, ***P < 0.001. (F) MYO1F and MYO1E gene expression pooled from tumor tissues and normal tissues of same patient (TCGA database). Pancreatic adenocarcinoma (PAAD): N (tumor) = 4, N (normal) = 4; LIHC: N (tumor) = 50, N (normal) = 50; LUSC: N (tumor) = 51, N (normal) = 51; LUAD: N (tumor) = 58, N (normal) = 58; COAD: N (tumor) = 40. P values were analyzed by nonparametric Wilcoxon matched-pairs signed rank test, *P < 0.05, **P < 0.01, ***P < 0.001. (G) B16F10 was transfected with a control shRNA construct or shRNA-Myo1f construct. After 48 h of treatment, cell lysates were prepared and probed with antibody against MYO1F by immunoblotting. (H) Tumor growth curve over time. MC38 was transfected with a control shRNA construct or shRNA-Myo1f construct, then subcutaneously injected with 1 × 106 cells on C57BL/6 mice (N = 10). Data were analyzed by one-way ANOVA test; ns, no significance. (I) Tumor collection at day 30 after tumor inoculation (N = 10 in each group). Data in H and I represent one experiment of three indep



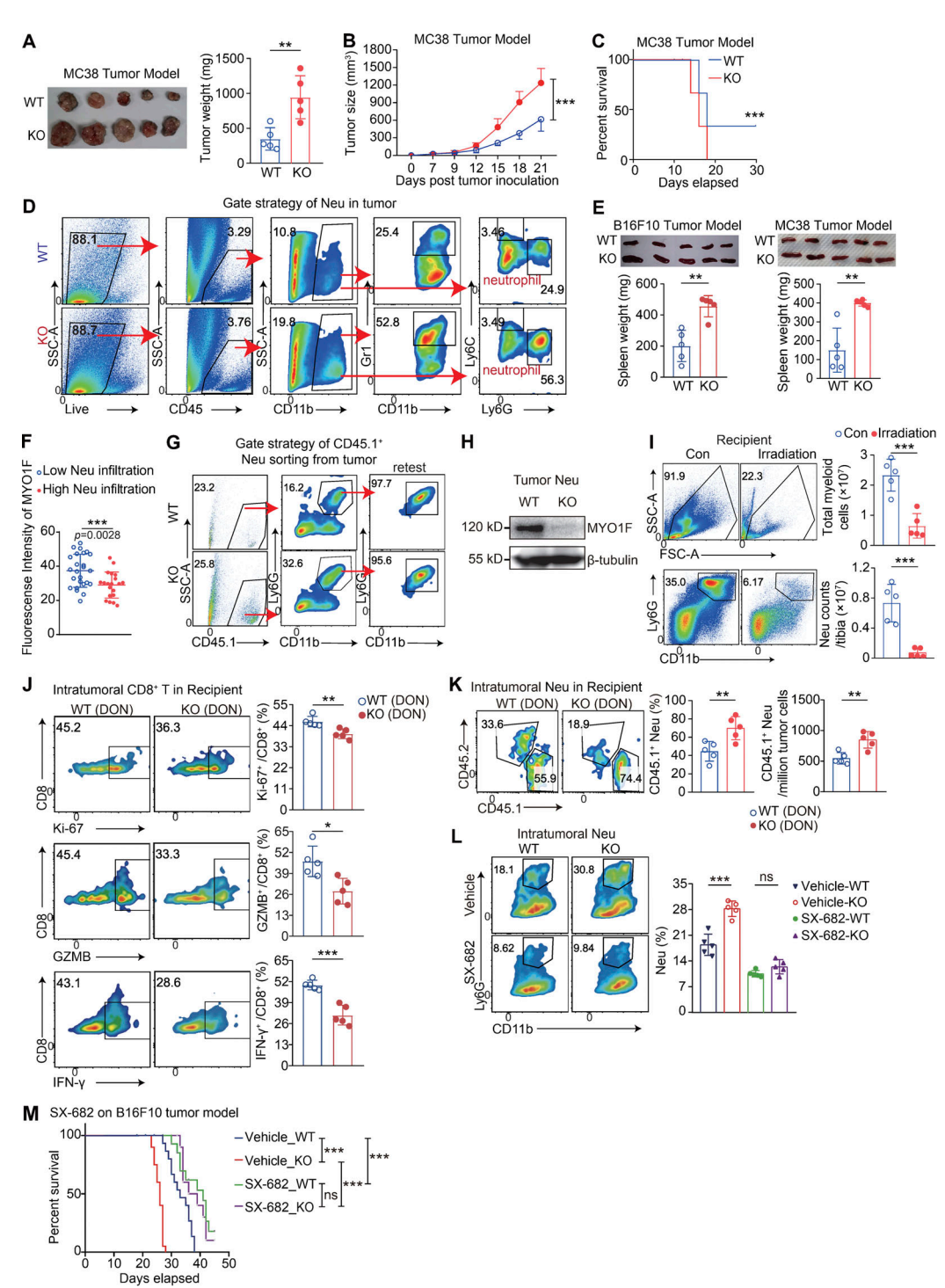


Figure S2. **MYO1F-KO** neutrophil promoted tumor growth and inhibited anti-tumor response of CD8* T cells. (A) WT and $Myo1f^{-/-}$ C57BL/6 mice were subcutaneously injected with 1×10^6 MC38 cells; tumor collection at day 21 (N = 5). (B) Tumor growth curve over time (N = 5). (C) Kaplan-Meier survival curves of MC38 tumor models (N = 10 in each group). (D) Gate strategy of tumor-infiltrating neutrophil flow sorting. (E) Spleen weight in B16F10 and MC38 tumor models of WT and $Myo1f^{-/-}$ mice. (F) Immunofluorescence intensity of MYO1F analyzed by Image]; low and high were distinguished artificially according to the number of infiltrations. N (Low Neu infiltration) = 25, N (High Neu infiltration) = 20. (G) Gate strategy of intratumoral CD45.1* neutrophil sorting from tumor. (H) Cell lysates of sorted tumor neutrophils were prepared and probed with antibody against MYO1F by immunoblotting. (I) Left: Gate strategy of the presence of total myeloid cells and neutrophils in BM at day 11 after irradiation without intervention. Right: Statistic of total myeloid cell and neutrophil counts in one tibia (N = 5). (J) Left: FACS analyses of intratumoral CD8* (IFN- γ *, GZMB*, and Ki-67*) cells from tumor tissues. Right: Statistical analysis. (K) FACS analyses of intratumoral CD11b*Ly6G* neutrophils from recipient tumor tissues. Right: Statistic of proportion and counts of neutrophils. (L) FACS analyses of intratumoral CD11b*Ly6G* neutrophils from tumor tissues. (M) Kaplan-Meier survival curves of SX-682-treated B16F10 tumor models (N = 20 in each group). Data in A-E and G-L represent one experiment of three independent repeats; F represents one experiment of two independent repeats. Data are presented as mean \pm SD. P values were analyzed by one-way ANOVA test (B, L, and M); log-rank (Mantel-Cox) (C); two-tailed unpaired Student's \pm test (A, E, F, and I-K), *P < 0.05, **P < 0.01, and ***P < 0.001. ns, no significance. Neu, neutrophil. Source data are available for this figure: SourceData FS2.



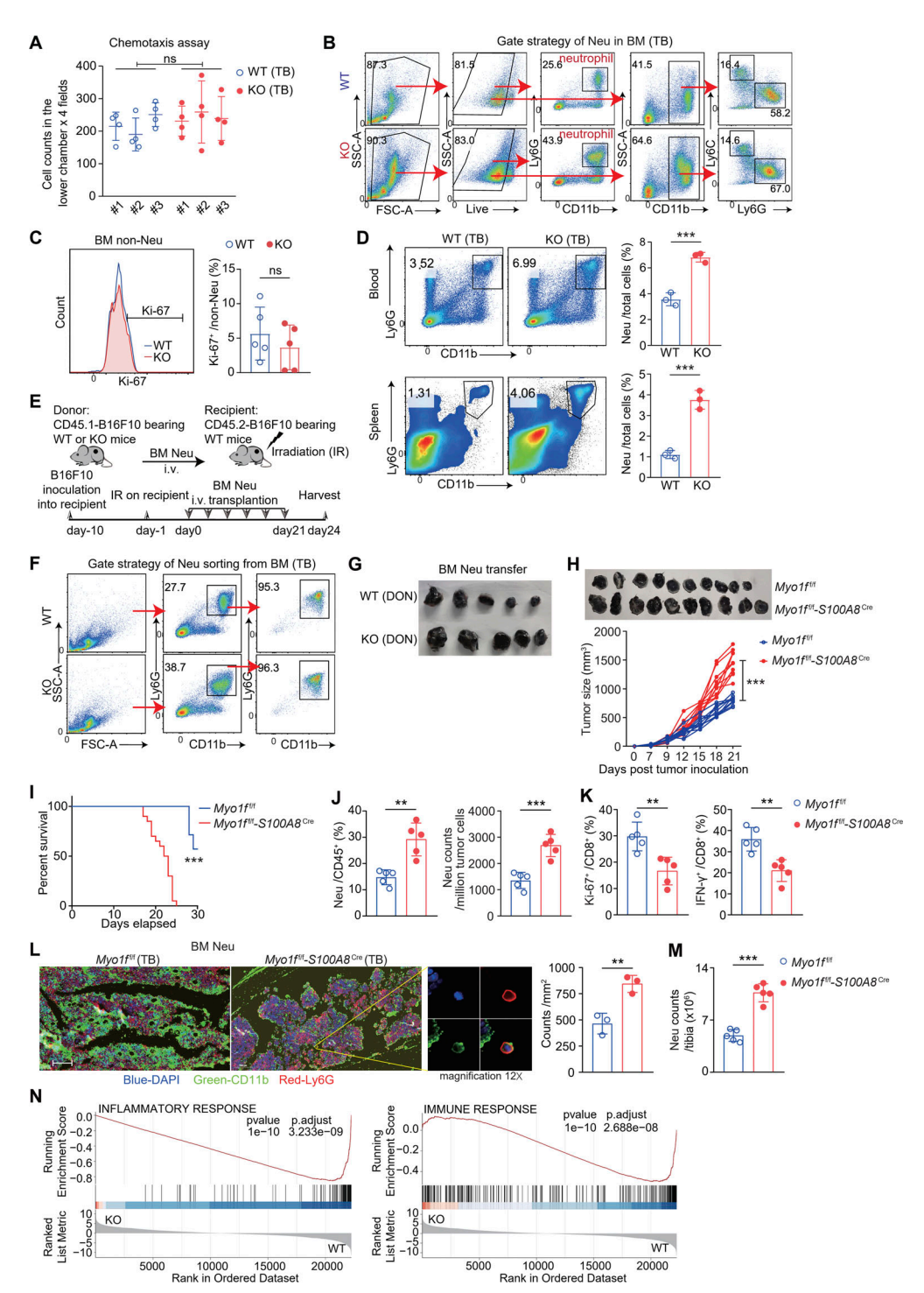


Figure S3. **MYO1F-deficient neutrophil suppressed immune response during tumor progression. (A)** Cell migration ability evaluated by chemotaxis transwell induced by CXCL2; passed cells adhered to the lower chamber surface were counted. **(B)** Gate strategy of BM neutrophils from B16F10 tumor model at day 21. **(C)** FACS analyses of Ki-67 in CD45+Ly6G⁻ clusters from BM of WT and $Myo1f^{-/-}$ B16F10 tumor models at day 21 (N = 5). **(D)** FACS analyses of neutrophils in peripheral blood and spleen from B16F10 tumor model at day 21 (N = 3). **(E)** Schematic of BM neutrophils transfer from donor (CD45.1 B16F10 tumor-bearing WT or KO mice) to recipient (CD45.2 WT mice). **(F)** Gate strategy of BM neutrophils sorting from B16F10 tumor model at day 21. **(G)** Tumor collection at day 20 after tumor inoculation. **(H)** Top: Tumor growth curve over time. Bottom: Tumor collection at day 21 after tumor inoculation (N = 10). **(I)** Kaplan-Meier survival curves (N = 20). **(J)** FACS analyses of intratumoral CD11b+Ly6G⁺ neutrophils from tumor tissues (N = 5). **(K)** FACS analyses of intratumoral CD8+ (IFN- γ + and Ki-67+) cells from tumor tissues (N = 5). **(L)** Left: Immunofluorescence staining of CD11b (green) and Ly6G (red) in BM from B16F10 models. Right: Statistic of numbers by counting colocalization (N = 3). Scale bar: 200 μ m. **(M)** Counts of total CD11b+Ly6G+ neutrophils in one tibia by FACS (N = 5). **(N)** Gene set enrichment analysis of inflammatory response signaling pathway and immune response signaling pathway. Data in A-J and L represent one experiment of three independent repeats; K and M represent one experiment of two independent repeats. Data are presented as mean \pm SD. P values were analyzed by one-way ANOVA test (H); log-rank (Mantel-Cox) (I); two-tailed unpaired Student's \pm test (A, C, D, and J-M), *P < 0.05, **P < 0.01, and ***P < 0.001. ns, no significance; Neu, neutrophil; TB, tumor bearing.



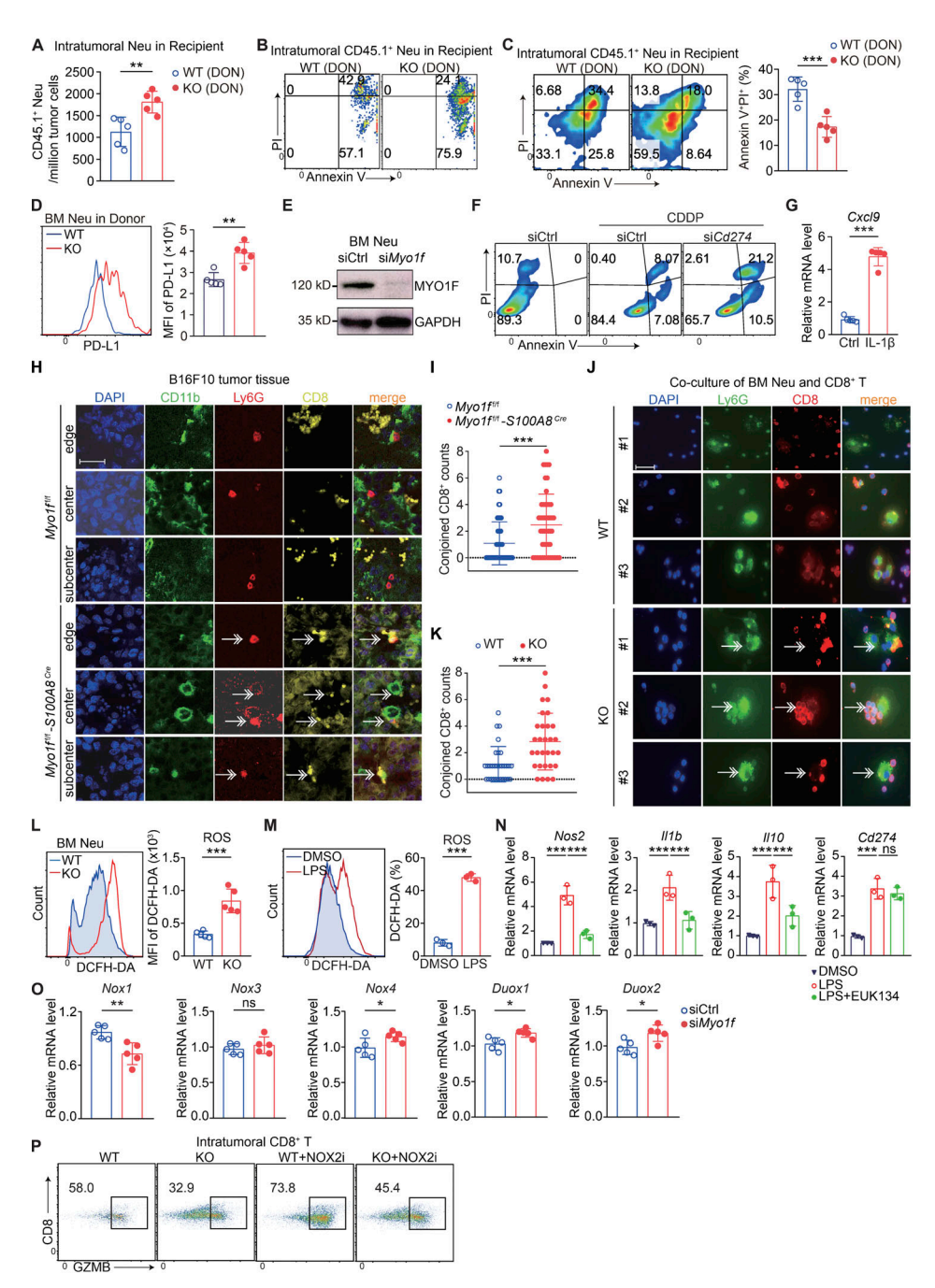


Figure S4. The absence of MYO1F in neutrophils leads to delayed apoptosis and increased recruitment of CD8* T cells. (A) Counts of intratumoral CD11b+Ly6G+ neutrophils in recipient by FACS (N = 5). (B and C) FACS analyses of apoptosis of intratumoral CD11b+Ly6G+ neutrophils by staining with annexin V and PI. (D) FACS analyses of PD-L1 on BM neutrophils from WT and Myo1f-/- B16F10 tumor models at day 21 (N = 5). (E) Cultured neutrophils from WT were transfected with siMyo1f (20 pM); MYO1F protein levels were analyzed 48 h after transfection by immunoblotting. (F) Cultured neutrophils from WT were transfected with siCtrl or siCd274 (20 pM); FACS analyses of apoptosis of neutrophils by staining with annexin V and PI after induction of cisplatin (2 μM) (N = 5). (G) Cxcl9 mRNA levels were detected by qPCR from cultured neutrophils treated with IL-1β (50 ng/ml) (N = 5). (H) Immunofluorescence staining of CD11b (green), Ly6G (red), and CD8 (yellow) in B16F10 tumor models at day 20. 50 representative images for each group were counted (white arrow, co-binding site). Scale bar: 50 μm. (I) Statistic of combination numbers of CD8+ T and CD11b+Ly6G+ neutrophils by counting colocalization. N = 50 per group. (J) Immunofluorescence staining of Ly6G (green) and CD8 (red) in co-culture of CD8⁺ T cell and CD11b⁺Ly6G⁺ neutrophils. 30 representative images for each group were counted (white arrow, co-binding site). Scale bar: 50 μm. (K) Statistic of combination numbers of CD8+T cell and Ly6G+ neutrophils by counting colocalization. N = 30 per group. (L) FACS analyses of ROS in BM neutrophils by labeling DCFH-DA. Neutrophils from WT and Myo1f-/- B16F10 tumor models at day 21 (N = 5). (M) FACS analyses of ROS in cultured neutrophils by labeling DCFH-DA after induction of LPS (500 ng/ml) for 18 h (N = 5). (N) Cultured WT neutrophils were treated with EUK-134 (20 μM) for 12 h and induced with LPS (500 ng/ml) for another 18 h; Nos2, II1b, II10, and Cd274 mRNA levels were detected by qPCR (N = 5). (0) Nox1, Nox3, Nox4, Duox1, and Duox2 mRNA levels were detected by qPCR from WT cultured neutrophils at 48 h after transfection of siRNA (N = 5). (P) FACS analyses of intratumoral CD8+ (GZMB+) cells from tumor tissues. Data in A-P represent one experiment of three independent repeats. Data are presented as mean ± SD. P values were analyzed by one-way ANOVA test (N); two-tailed unpaired Student's t test (A, C, D, G, I, K-M, and O), *P < 0.05, **P < 0.01, and ***P < 0.001. ns, no significance. Neu, neutrophil. Source data are available for this figure: SourceData FS4.



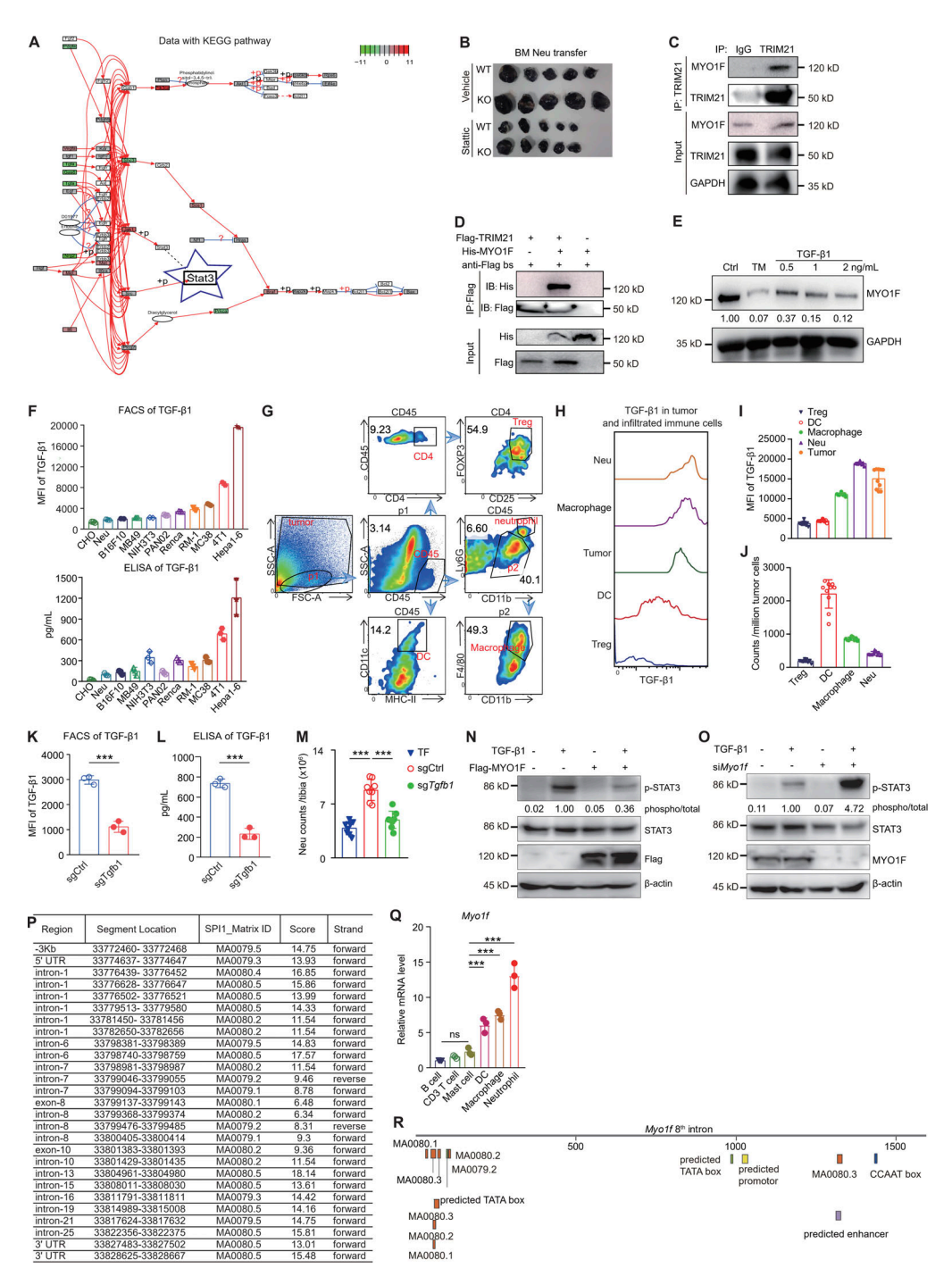


Figure S5. **Tumor-derived TGF-β1 promoted STAT3 activation by inhibiting Myo1f expression. (A)** KEGG pathway. Blue star indicates phospho-STAT3 signaling. **(B)** Tumor collection at day 27 (N = 5). **(C)** Endogenous IP (co-IP) blot with BM neutrophils from WT mice, where IP was performed for TRIM21, and then precipitates were immunoblotted (IB) with an anti-MYO1F antibody. **(D)** Exogenous co-IP blot with transfection of Flag-tagged TRIM21 and His-tagged MYO1F in 293T, where IP was performed for Flag, and then IB with an anti-His antibody. **(E)** Cultured WT neutrophils was treated with TGF-β1; MYO1F protein levels were analyzed 72 h after treatment by immunoblotting. **(F)** Top: FACS analyses of cytoplasmic TGF-β1 in different cell lines and neutrophils. Bottom: ELISA analysis of TGF-β1 from supernatant of cell lines. **(G)** Gate strategy of intratumoral immune cells from WT B16F10 tumor model. **(H and I)** FACS analyses of cytoplasmic TGF-β1 in different tumor-infiltrated immune cells and statistics of TGF-β1 MFI level. **(J)** Statistics of immune cells in total tumor cells as described in H. **(K and L)** FACS analyses of cytoplasmic TGF-β1 in B16F10 cells transfected with sgCtrl or sg*Tgfb1*; ELISA analysis of TGF-β1 from supernatant of B16F10 cells (N = 3). **(M)** Counts of total CD11b⁺ Ly6G⁺ neutrophils in one tibia by FACS (N = 5). **(N)** Detecting STAT3 phosphorylation level of cultured neutrophils with overexpression of Flag-tagged MYO1F through western blotting, ratio of phosphor-STAT3 to total STAT3 was shown in the middle. **(P)** SPI1-binding sites on *Myo1f* predicted by JASPAR. **(Q)** *Myo1f* mRNA levels were detected by qPCR from sorted immune cells (N = 3). **(R)** Transcription-related sites and SPI1-binding sites predicted by Softberry. Data in B-O and Q represent one experiment of three independent repeats. Data are presented as mean ± SD. P values were analyzed by one-way ANOVA test (M and Q); two-tailed unpaired Student's t test (K and L), *P < 0.05, **P < 0.01, and ***P < 0.001. ns, no significance